Parametrized Simulation of Charge Drift and Collection in the nEXO TPC

by

Alexander Lars Robinson

A thesis submitted in partial fulfillment
of the requirements for the degree of
Master of Science (MSc) in Physics

The Faculty of Graduate Studies
Laurentian University
Sudbury, Ontario, Canada

THESIS DEFENCE COMMITTEE/COMITÉ DE SOUTENANCE DE THÈSE
Laurentian Université/Université Laurentienne
Faculty of Graduate Studies/Faculté des études supérieures

Title of Thesis Titre de la thèse	Parametrized Simulation of Charge Drift and Collection in the nEXO TPC
Name of Candidate Nom du candidat	Robinson, Alexander Lars
Degree Diplôme	Master of Science
Department/Program Département/Programme	Physics
Date of Defence Date de la soutenance	mars 13, 2019

APPROVED/APPROUVÉ

Thesis Examiners/Examinateurs de thèse:

Dr. Jacques Farine
(Supervisor/Directeur de thèse)

Dr. Ubi Wichoski
(Committee member/Membre du comité)

Dr. Caio Licciardi
(Committee member/Membre du comité)

Dr. Blair Jamieson
(External Examiner/Examinateur externe)

Approved for the Faculty of Graduate Studies
Approuvé pour la Faculté des études supérieures
Dr. David Lesbarrères
Monsieur David Lesbarrères
Dean, Faculty of Graduate Studies
Doyen, Faculté des études supérieures

ACCESSIBILITY CLAUSE AND PERMISSION TO USE

Abstract

For the purpose of creating a computationally fast and light-weight simulation of charge drift, diffusion, and collection in the nEXO TPC, a numerical Python package was developed which implements two different models. The models implemented are: diffusion via fragmentation of a charge cloud into point charges, and diffusion via integration of the idealized Gaussian distribution across the anode's charge-collection pads. Both methods are described in detail, and the latter is compared to a more detailed simulation.

***Keywords* —** nEXO, TPC, simulation, charge drift, charge diffusion, charge tiles, error function

Contents

List of Tables

List of Figures

1 Introduction

1.1 Motivation

The neutrino was first hypothesised by Pauli in 1930 to explain the continuous energy spectra of the electrons emitted by beta-decays, maintaining the conservation of momentum and energy [1]. Since the spectrum (and further evidence) requires the neutrino to have negligible mass relative to the electron, and since there has been no immediately obvious mechanism by which a suitably small mass would arise, the Standard Model of particle physics has historically treated the neutrino as a massless particle.

Measurements of neutrino oscillation [2, 3], however, show that the neutrinos must have non-zero mass-eigenstates, such that differently-massive components may drift out of phase with weak-interaction eigenstates. These oscillations cannot measure the neutrino mass directly, and can only measure the squared differences in mass between mass eigenstates. A number of possibilities for experimentally measuring various aspects neutrino mass exist, including direct measurement of the electron neutrino mass (an expectation value) in beta-decay spectra, and supernova-timing measurements. Of particular interest here is the potential method of measuring neutrino mass through *neutrinoless double beta-decay*, a phenomenon which would be possible if neutrinos were *Majorana fermions*.

The property of mass provides a mechanism to distinguish between two possible formulations of the neutrino: the Dirac formulation, wherein neutrinos and anti-neutrinos are distinct solutions each with two spin solutions (one of which is “sterile” due to the chirality of the weak interaction);

and the Majorana formulation, wherein the anti-neutrino solution is equivalent to the right-handed solution for the otherwise left-handed neutrino.

In both formulations, the mass of the neutrino allows its handedness to flip (or be perceived as flipped in another frame of reference); for Majorana neutrinos, this would open the door for the violation of lepton-number conservation in interactions, as well as other potential new physics. For example, if the neutrino mass has *both* Dirac and Majorana terms, this may allow for a small neutrino mass through a "see-saw" mechanism, whereby a light neutrino mass-eigenstate exists alongside a much more massive sterile neutrino mass-eigenstate [4]. These prospective heavy sterile neutrinos have also been suggested as a dark matter candidate.

1.2 Neutrinoless Double Beta-Decay

Double beta-decay (*ββ-decay*) is the process by which a forbidden beta-decay into an unfavourable higher-energy intermediate isotope may be skipped by a decaying nucleus, by performing two beta-decays simultaneously (within time-energy uncertainties). While ββ-decay is technically also possible for isotopes where the intermediate is *not* unfavourable, it will be accompanied by an overpowering background of regular single beta-decays, making it far less convenient to study. The emission of two anti-neutrinos will, as with a single beta-decay, carry energy away from the decay, reducing the energy of the two electrons to produce a broad spectrum of total kinetic energy, from zero to the full energy of the decay.

An example of a possible violation in lepton-number conservation by Majorana neutrinos includes *neutrinoless double beta-decay* (0νββ). This differs from a normal two-neutrino double beta-decay (2νββ) in that, rather than lose decay-energy to the emission of anti-neutrinos, a virtual Majorana neutrino is emitted (as an anti-neutrino), and absorbed (as a neutrino), preserving the energy of the decay in the more directly-measurable pair of electrons. Thus the electron energy spectrum of 0νββ is *monoenergetic*.

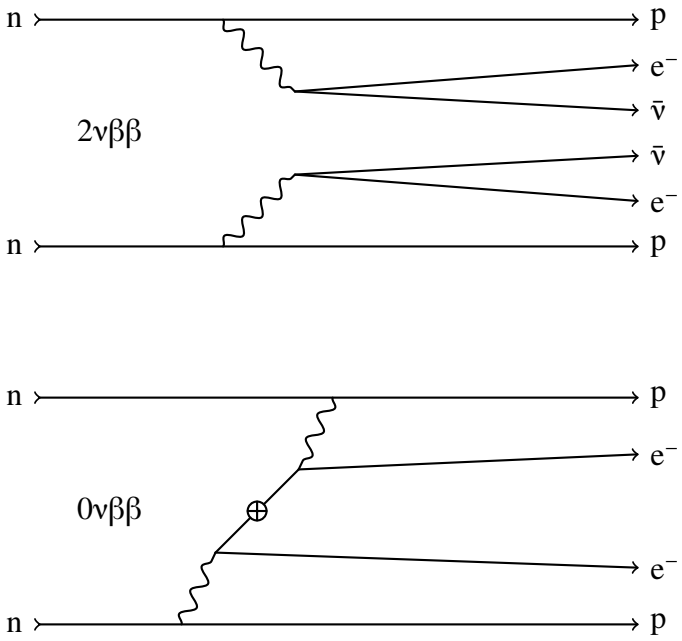

Figure 1: Feynman diagrams for 2νββ (top) and 0νββ (bottom). The ⊕ represents a Majorana-$\bar{\nu}$ changing handed-ness, becoming a Majorana-ν.

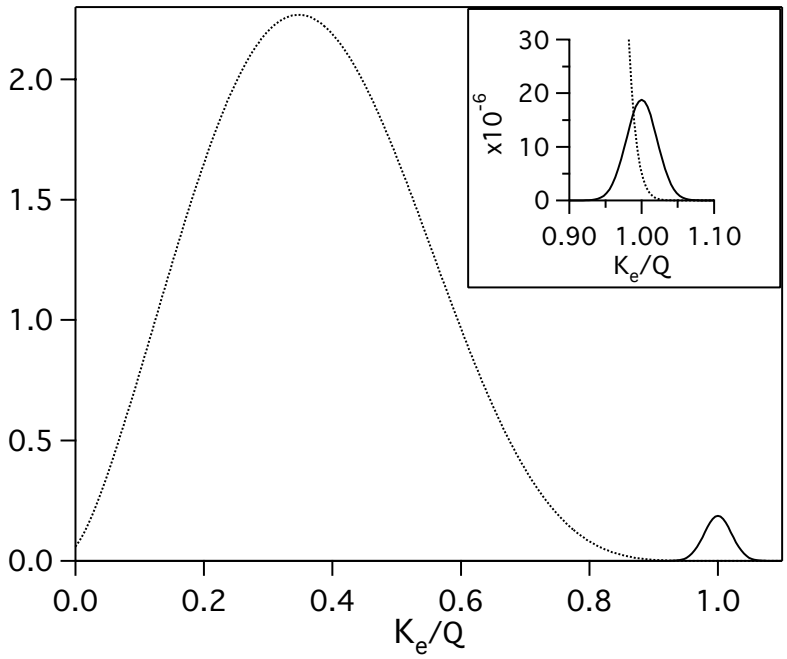

Figure 2: Example energy spectrum of 0νββ (solid) compared to 2νββ (dotted), reproduced from [5]. The 0νββ spectrum is normalized to 10^{-2} (10^{-6} in the inset) relative to 2νββ, with a 5% energy resolution.

This decay mode, if it exists, should therefore be detectable in the ββ-decay energy-spectrum of a candidate element as an additional monoenergetic peak, and its half-life would be related to the Majorana neutrino mass as follows:

$$\left[T_{1/2}^{0\nu}\right]^{-1} = G^{0\nu} \cdot \left| {g_A}^2 \cdot M_{GT}^{0\nu} - {g_V}^2 \cdot M_F^{0\nu} + {g_A}^2 \cdot M_T^{0\nu} \right|^2 \cdot \frac{\langle m_{\beta\beta} \rangle^2}{{m_e}^2} \tag{1}$$

where $T_{1/2}^{0\nu}$ is the 0νββ half-life, $\langle m_{\beta\beta} \rangle$ is the effective Majorana neutrino mass, m_e is the electron mass, $G^{0\nu}$ is a phase-space factor, the $M^{0\nu}$ are nuclear matrix elements (Gamow-Teller, Fermi, and tensor), and the g are weak-interaction coupling constants (axial-vector and vector) [4]. This includes 0νββ, should it occur, as a possible means of directly measuring the neutrino mass scale. This is, however, dependent on the values of the nuclear matrix elements, which must be calculated from theory, as well as variation in the coupling constants [6–8]. Additionally, depending on whether neutrinos are purely Majorana fermions or instead have a composite mass term (for example, as with the see-saw mechanism), this measurement may serve either as a measurement of the electron-neutrino mass, or instead merely as a measurement of its Majorana component.

1.3 Experimental Approach

Because of the potential for a measurement of the Majorana mass component of the electron neutrino, a number of collaborations and projects have been searching for 0νββ over the past several decades. Several recent and planned examples are listed in Table 1. A diversity of ββ-decay candidates have been tested under increasingly high precision, with a significant proportion of the attention being devoted to ^{76}Ge, ^{130}Te, and ^{136}Xe [6–8].

Germanium can be formed into high purity semiconductor crystals, which can then be built into charge-detecting diodes. Similarly, tellurium dioxide (TeO_2) crystals can be used directly as part of a *bolometer*, which measures changes in the heat energy of the crystal through changes in its electrical resistance. In both cases, the source doubling as the electrically-instrumented detector yields a very good energy resolution, but little information about the topology of events [7, 8].

Xenon, on the other hand, being a noble gas, is relatively inexpensive to purify and enrich, making it well suited for large-scale low-background applications. However, it requires external instrumentation, such as in a *time-projection chamber* (*TPC*), which collects and measures charge deposits (freed electrons) through drift in an applied electric field. Through the instrumentation of the anode and the distribution of the arrival time, a comparatively large amount of information can be obtained about the topology of each event, aiding in background reduction. For example, gamma-ray events, which, through Compton scattering, tend to leave multiple distinct clusters of deposits, can be distinguished from the more tightly grouped deposits of ββ-decay events, and so a large proportion can be discarded during analysis [4]. Additionally, some drift media, such as liquid xenon, will also scintillate in response to energetic particles. Using photomultipliers, this can be used to establish the exact time of occurrence of an event, and from the arrival time of the charge, the event's distance from the anode can also be measured.

Additionally, these and other isotopes can be employed either as sources for calorimeters (with trackers), or in a *loaded liquid scintillator*, where some concentration of the source isotope is dissolved into a large volume of high-purity scintillator fluid [6–8].

1.4 EXO

The *Enriched Xenon Observatory* (*EXO*) project is a series of ββ-decay collaborations using liquid xenon (*LXe*) heavily enriched in ^{136}Xe, the ββ-decay candidate with a decay energy at 2.458 MeV [20].

The *EXO-200* detector is a double time-projection chamber (*TPC*), symmetric about a central cathode, with an active mass of 110 kg of LXe (out of a 200 kg total inventory), enriched to 80.6% in ^{136}Xe, and which initially became operational in 2011 [21]. As of 2018, EXO-200 has placed limits of 147 to 398 meV on $\langle m_{\beta\beta} \rangle$ [12], and set leading limits on the half-lives of 2νββ and 0νββ in ^{134}Xe [22]. Because of EXO-200's success in using enriched xenon in a TPC, the vastly upscaled *nEXO* detector was put into planning.

Recent and Planned Experiments in $0\nu\beta\beta$

Isotope	Collaboration	Location	Mass (Source)	Detector Type	Phase	Starting Year	Active Years[a]	Sensitivity ($\langle m_{\beta\beta}\rangle$, meV)[b]
^{76}Ge	Majorana	SURF	29.7 kg (enr. Ge)	Ge crystals	demonstrator operational	2015	2	240 - 520
^{130}Te	CUORE-0	LNGS	39 kg (TeO_2)	TeO_2 crystal	completed	2013	2	270 - 760
^{76}Ge	GERDA II	LNGS	40 kg	Ge crystals	operational	2015	3	120 - 260
^{136}Xe	EXO-200	WIPP	200 kg (enr. Xe)	LXe TPC	completed	2011	7	147 - 398
^{136}Xe	KamLAND-Zen	Kamioka Obs.	348 kg (enr. Xe)	loaded liquid scintillator	operational	2011	5	61 - 165
^{136}Xe	NEXT	LSC	100 kg (enr. Xe)	LXe TPC	planning	2018	10	20 - 100 (predicted)
^{82}Se	SuperNEMO	LSM	100 kg (enr. Se)	tracker & calorimeter	demonstrator operational	2017	5	50 - 100 (predicted)
^{130}Te	CUORE	LNGS	742 kg (TeO_2)	TeO_2 crystal	operational	2017	5	40 - 100 (predicted)
^{130}Te	SNO+	SNOLAB	2340 kg (nat. Te)	loaded liquid scintillator	planning	2018	5	40 - 90 (predicted)
^{136}Xe	nEXO	TBD	5000 kg (enr. Xe)	LXe TPC	planning	TBD	10	5.7 - 17.7 (predicted)

[a] For operational and planned experiments, indicates the time needed to achieve the stated sensitivity.
[b] Upper limit for $\langle m_{\beta\beta}\rangle$; a range of limits is given, depending on and illustrating the effect of the choice of nuclear matrix elements.

Table 1: A brief overview of several $0\nu\beta\beta$ experiments, either recent or in planning. See [6–19] for references.

The nEXO detector is to be a monolithic TPC, filled with approximately 4000 kg of LXe (out of an approximately 5000 kg inventory), enriched to 90% in ^{136}Xe [4]. Owing to its large active mass, about 36 times that of EXO-200 (before accounting for the increased enrichment), the sensitivity to $0\nu\beta\beta$ will be much greater, in the range of 5.7 to 17.7 meV, an order of magnitude improvement over present limits [19]. The choice of a monolithic TPC design will also reduce backgrounds by moving the metal cathode from the center of the detector, increasing the fraction of the xenon volume distant from radioactive material impurities.

The TPC will consist of a cylindrical tank with a length and diameter of approximately 1.3 m. The cylinder will have a constant drift field along its axis, produced by an anode and cathode at opposite ends of the cylinder, aided by field-shaping rings distributed across the length. The detector will be instrumented with silicon photomultiplier staves along the cylinder wall to measure scintillation, and with charge readout tiles making up the anode, to measure free charge [4].

1.5 nEXO Simulations

In support of designing the nEXO detector, tools have been built to simulate the response of the TPC in operation. The primary element of the detector simulations is a Geant4 [23] application, the `nEXO_MC` application, which implements a simulation of the detector materials and geometry with which particle events, such as from nuclear decay, may interact. This application primarily outputs ROOT [24] files listing where and how much energy was deposited in the LXe by each event, but using the external *Noble Element Simulation Technique* (*NEST*) [25] library it can optionally output more details such as the resulting charge and light produced by each deposit. NEST is much more computationally expensive than the Geant4 application alone, and so is typically left disabled unless a more comprehensive simulation is required.

A detailed simulation of charge drift and collection exists [26, 27], but as with NEST it is computationally demanding. This detailed simulation drifts individual electrons (as produced by NEST) in the LXe, and simulates the time-varying charge their presence induces on the surfaces of the

anode elements. The resulting current, convoluted into the electronics response, is taken as that element's *current waveform*, which can be integrated to calculate the total collected charge for that element. Electronics noise is also included in the current and charge waveform simulation.

For the sake of computational efficiency, a simplified simulation of charge collection is desired. An *especially* simplified version already exists as an external Python script, which does not compute charge drift, diffusion, or collection, but only "clusters" deposits within a given characteristic radius as a measurement of event-width. To provide a fast simulation that accounts for the features of charge drift through the LXe and collection by the anode, the `readout` package has been developed, implementing diffusion and collection by two differing algorithms sharing a control mechanism.

1.6 `readout` Package

The purpose of this *Python* [28] application is to take deposits of energy in liquid xenon (LXe) in the TPC, and translate them into energy signals on the TPC anode, appropriately distributed in space and time. Other scripts and applications can then be used to analyze the output. This package and its auxiliaries make heavy use of the *SciPy* (*Scientific Python*) [29] and *NumPy* (*Numerical Python*) [30] libraries, as well as the data-structuring library *Pandas* [31] and the plotting library *Matplotlib* [32].

The `readout` application was initially based on a rewrite of an older prototype Python script implementing the fragmentation algorithm, wherein diffusion is approximated by fragmenting charge deposits into a shower of point charges (Section 2). This prototype performed calculations one deposit at a time in pure Python, which was inefficient, and further compounded by other optimization flaws, such as the parsing of a certain numerical function from a text string upon every (very frequent) use. To resolve this, the script was *vectorized*, replacing looped operations in Python with a single operation on arrays (vectors), using the NumPy library, to more efficiently

perform batch calculations with precompiled loops. This vectorization and further optimization resulted in a run-time improvement by a factor of fifteen.

This vectorized script was then completely rewritten as an object-oriented Python package (the `readout` package) to improve readability and modularity. This allowed the implementation of the Gaussian integration algorithm, in which deposits are diffused by integrating the analytical Gaussian distribution across volume elements (Section 3), providing an alternative to the original. Further optimizations in the aggregation of energy on the TPC anode using sorting algorithms provided by the Pandas data-analysis library yielded another factor of two of improvement in run-time.

The `readout` package has since undergone several rounds of validation (Section 4), both to ensure sensible output and to confirm its utility as a simpler but faster alternative to the detailed charge simulation. This has shown that, with proper consideration given to the constraints of a real detector (or a comprehensive simulation thereof), the output of the `readout` package can very closely match the output of the comprehensive simulation when using identical drift and collection parameters.

By default, data is input to and output from the `readout` package via ROOT files, while parameters are specified using a ”card file” system, in which a text file of parameters are listed with their values. This card file is read into a Python dictionary object, which is used to initialize objects by keyword parameters. The package has been organized such that other I/O methods could be substituted with relative ease.

The charge deposits to be drifted are typically parametrized in terms of equivalent energy; this is primarily a choice of units: should all values expecting units of energy be substituted with values of charge, the output values will be the charge collected, rather than the energy detected. The average energy per electron (the inverse of the charge yield) is the constant of proportionality between these two regimes, but needs to be determined independently. Initially, this was chosen as the *w-value*

of liquid xenon (15.6 eV per electron [33]); however, it was suggested that, as the value in the limit of an infinite electric field, this was significantly too low for the 100 to 500 V cm regime planned for nEXO [27], so a value of 25 eV per electron has been estimated from NEST benchmark plots instead [34].

Since a *precise* conversion of energy deposits into free electrons (by NEST) is computationally intensive, the energies deposited directly into in the LXe by the Geant4 application are typically processed instead. Since these energies are what NEST ultimately divides between charge and scintillation (and also heat), this means that, without NEST, energy-loss to scintillation is ignored, though scintillation is still assumed to exist as a near-instant indicator of the starting time of drift.

2 Fragmentation Algorithm

This algorithm treats LXe energy deposits as groups of point charges, and hence must handle diffusion similarly. This is accomplished by dividing each energy deposit into a number of smaller fragments, each carrying an equal fraction of the total energy deposited. The algorithm selects, for each deposit, the smallest number of fragments such that each fragment's energy is lower than the maximum fragment size (a free parameter chosen by the user). If this fragment size were selected such that it was on the order of magnitude of the average energy represented by each drifting electron (in the vicinity of 25 eV per electron), this algorithm would begin to approximate the behaviour of an actual electron cloud. However this would both defeat the purpose of a "fast" simulation and lack several considerations one might desire in a "full" simulation, such as the effects of the charge of the electron cloud itself, surface charge induced on the anode, and so on.

2.1 Diffusion

The diffusion at time t of a particle undergoing a random walk can be described along an axis w using a Gaussian probability distribution function:

$$w = w_0 + n\sqrt{2D_w t} \tag{2}$$

where n is a random normal deviate, w_0 is the starting point, and D_w is the diffusion coefficient along w. This produces a Gaussian distribution with a mean of w_0 and a standard deviation of $\sqrt{2D_w t}$ (this detail will be revisited in Section 3.1.1).

Along the x and y axes of the anode, the diffusion coefficient of electrons is a single *transverse* diffusion coefficient D_t. Along the z axis, electrons are additionally drifting towards the anode at drift speed v_d under a constant electric field, and diffuse with a different (smaller) *longitudinal* diffusion coefficient D_l. Additionally, the z position is not measured directly, but instead through the time of arrival at the anode, resulting in a complication where t appears dependent on itself:

$$t = \frac{z}{v_d} = \frac{z_0 + n\sqrt{2D_l t}}{v_d} \tag{3}$$

This can be rewritten as a quadratic equation in $\sqrt{t}$, and solved to produce

$$t = t_0 + 2\left(\xi^2 + \xi\sqrt{t_0 + \xi^2}\right) \tag{4}$$

where $t_0 = z_0/v_d$ and $\xi = (n/v_d)\sqrt{D_l/2}$.

In the region of the distribution where $\xi^2 \ll t_0$, this can be simplified to:

$$\begin{aligned} t &\approx t_0 + 2\xi\sqrt{t_0} \\ &= t_0 + n\sqrt{2\frac{D_l}{{v_d}^2}t_0} \\ &= \frac{z_0 + n\sqrt{2D_l t_0}}{v_d} \end{aligned} \tag{5}$$

which is similar to the transverse case, and effectively approximates the distribution cloud's arrival as instantaneous by substituting of $\sigma = \sqrt{2D_l t}$ with $\sigma = \sqrt{2D_l t_0}$. Since a Gaussian distribution is not finite, and since this requires that forward parts of the diffusion cloud be treated as diffusing more than in actuality, this provides an additional means of checking that this approximation is consistent, by ensuring that the region is small in which a significant part of the final collected distribution approximates as behind the anode, or, equivalently, as having a negative collection time.

The proximity z_p at which the 5σ boundary of the distribution intersects with the anode can be determined as the solution of

$$\begin{aligned} z_p &= 5\sqrt{2D_l\frac{z_p}{v_d}} \\ \therefore z_p &= 50\frac{D_l}{v_d} \end{aligned} \tag{6}$$

and since the width of the distribution scales with the square root of the distance z from the anode, we can guarantee that the unfavourable region is on the side of this boundary near to the anode, where $z_0 < z_p$. For example, using a longitudinal diffusion D_l of $0.0013\,\mathrm{mm^2\,\mu s^{-1}}$ and a drift velocity v_d of $1.705\,\mathrm{mm\,\mu s^{-1}}$ (see Table 2), z_p becomes 38 µm, which, for a 1.3 m TPC is a negligible fraction of the total drift length. In the case of the fragmentation algorithm, this approximation is generally unnecessary regardless, as the additional computational cost of Equation 4 is negligible. The approximation will be revisited in the case of the Gaussian algorithm (Section 3.1), however.

For an impure drifting medium, there will also be an exponential decay in the strength of the signal, as electrons are probabilistically captured:

$$E(t) = E_0 e^{-\frac{t}{\lambda}} \tag{7}$$

where λ is the mean lifetime of the electrons. Using the time obtained from Equation 4, this exponential factor can be applied to a fragment's energy immediately following diffusion, accounting for the exact amount of time the fragment has taken to reach the anode.

2.2 Anode

The anode planned for the nEXO TPC is to be built of identical square pads (3 to 6 mm wide each) linked by their corners into strips (about 10 cm long each), with orthogonally-aligned strips overlapping such that their pads form a checkerboard pattern (rotated 45 degrees). These overlapping

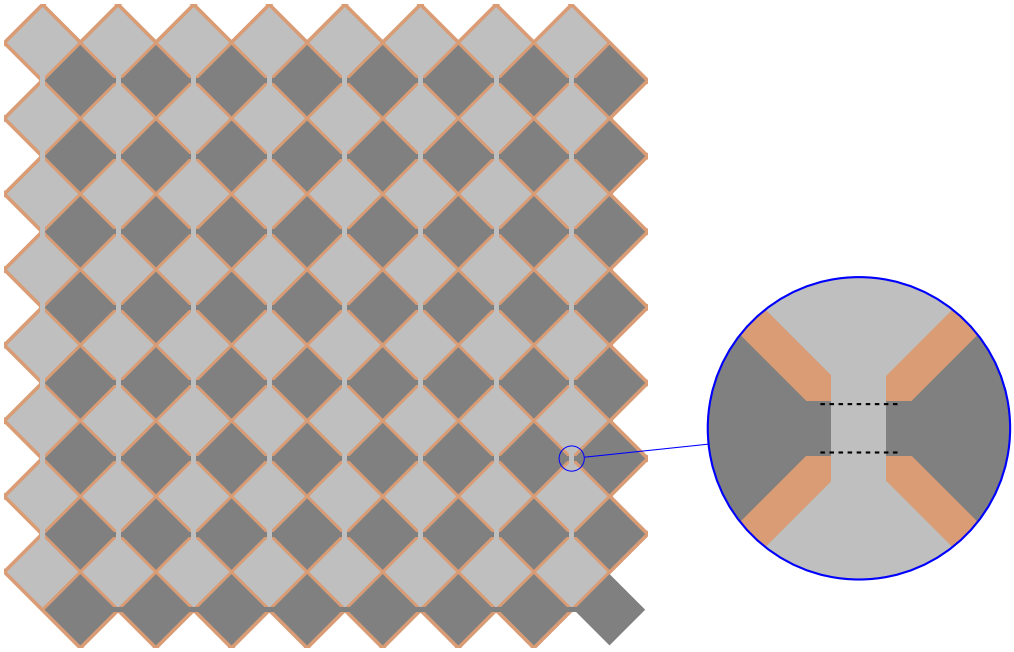

Figure 3: A simplified diagram of an example charge-collection tile with 8 pads per strip. Vertically connected x-strips (light grey) and horizontally connected y-strips (dark grey) overlap to cover a non-conductive substrate (tan). An (insulated) intersection between two strips is shown inset. Spacing between pads and widths of connecting wires have been greatly exaggerated in scale.

strips are then grouped into square tiles (Figure 3), such that the pad squares are diagonal to the tile square, and these tiles are what forms the anode and charge detector of the TPC [4].

The effect of this is that the two orientations of strips measure position diagonally to the grid formed by the pads. One can then use rotations to align the x and y coordinates of a collected deposit or fragment with that of the grid of pads, from which the pad can be determined, followed by the strip and tile through de-rotation. Assuming a convention of indexing strips such that the x-strip centered on and running along the y axis is indexed as x-strip 0 and vice-versa, with adjacent strips indexed by positive and negative integers along each axis, we can perform this discrimination as follows, and as illustrated in Figure 4.

Taking an x and y coordinate as a complex number r:

$$r = x + yi \tag{8}$$

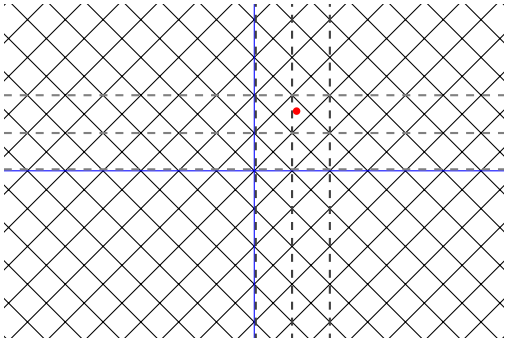

(a) A charge deposit or fragment (red) is collected on the anode's grid of pads. Nearby strips are marked with dashed lines.

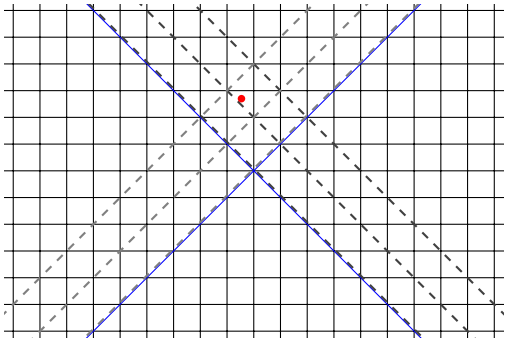

(b) The coordinate system is rotated to align with the grid of pads. (Equation 9)

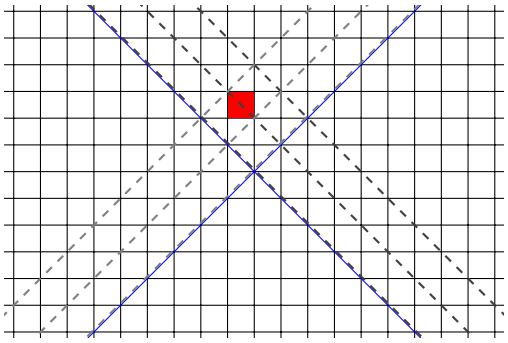

(c) The exact pad which collected the deposit is identified by flooring the position. (Equation 10)

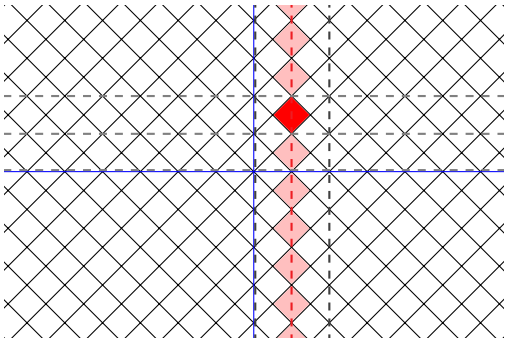

(d) The coordinate system is de-rotated, then the axis and position of the strip (pink) are determined from the position of the pad's center. (Equations 11 & 12)

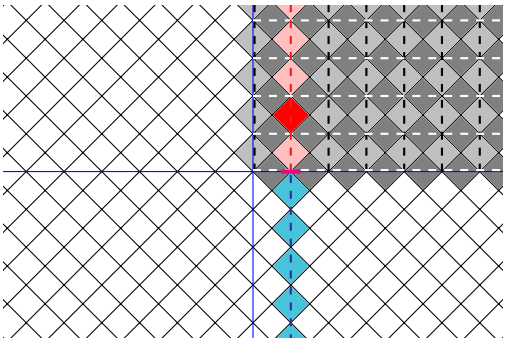

(e) The strip is further segmented into distinct tiles. The blue portion is not in this tile (grey). (Equations 14 & 15)

Figure 4: The process of discriminating the strip upon which an incident charge deposit lands, beginning from the diagonal grid of pads.

we can rotate the coordinate system 45 degrees clockwise with a multiplication (Figure 4b):

$$\begin{aligned} r_p &= (x + yi)\frac{(1+i)}{\sqrt{2}} \\ &= \frac{(x-y) + (x+y)i}{\sqrt{2}} \\ &= \frac{x_p + y_p i}{\sqrt{2}} \end{aligned} \tag{9}$$

We can then scale by pad size and take the floor along both axes to determine which pad, on an integer coordinate-grid, this point lies within (Figure 4c):

$$\begin{aligned} p &= \left\lfloor \frac{r_p}{w_p/\sqrt{2}} \right\rfloor \\ &= \left\lfloor \frac{x_p}{w_p} \right\rfloor + \left\lfloor \frac{y_p}{w_p} \right\rfloor i \\ &= p_x + p_y i \end{aligned} \tag{10}$$

The pad width w_p represents the diagonal width of a pad (also referred to as the pitch size), which is also the width of a strip. The sides of each square pad thus have a width of $w_p/\sqrt{2}$ which becomes the scaling factor before flooring.

Taking the center of each pad, we can rotate these back onto the original x and y axes (Figure 4d):

$$\begin{aligned} S &= \left(\left(p_x + \frac{1}{2}\right) + \left(p_y + \frac{1}{2}\right)i\right)\frac{(1-i)}{\sqrt{2}} \\ &= \frac{(p_x + p_y + 1) + (p_y - p_x)i}{\sqrt{2}} \\ &= \frac{S_x + S_y i}{\sqrt{2}} \end{aligned} \tag{11}$$

whereupon the centers have been scaled by $\sqrt{2}/w_p$ relative to the original coordinates. By omitting the factor of $1/\sqrt{2}$ in the second rotation, we have a total scaling factor of $2/w_p$, where exactly one of either S_x or S_y is even, with the other being odd. The even value can thus be divided by 2 to produce an integer strip-index S_{index} of the position of a strip along its measuring respective axis.

$$S_{index} = \begin{cases} S_x/2 & \text{if } 2 \mid S_x \\ S_y/2 & \text{otherwise } (2 \mid S_y) \end{cases} \tag{12}$$

$$\because S_y = S_x - 2p_x - 1 \tag{13}$$

We can also determine which *tile* a strip belongs to, using another floor after a scaling by the number of pads-per-strip n_p in a tile (as well as the aforementioned factor of 2) (Figure 4e).

$$\begin{aligned} T &= \left\lfloor \frac{S_x}{2n_p} \right\rfloor + \left\lfloor \frac{S_y}{2n_p} \right\rfloor i \\ &= T_x + T_y i \end{aligned} \tag{14}$$

Since the tile index along the strip-index direction can be determined from the latter at will, only the tile index orthogonal to the strip index (the tile index which determines how this strip is segmented across tiles) is kept and stored.

$$T_{index} = \begin{cases} T_y & \text{if } 2 \mid S_x \\ T_x & \text{otherwise } (2 \mid S_y) \end{cases} \tag{15}$$

The divisibility of S_x by 2 is determined through the use of the modulus operation (`%` in Python and C), the value of which is then used as a strip-axis indicator, with 0 for x-strips and 1 for y-strips. Additionally, following Equation 10, all calculations can be done purely with integers, improving performance and numerical stability. Example maps of how these indices vary over the anode are depicted in Figures 5, 6, and 7.

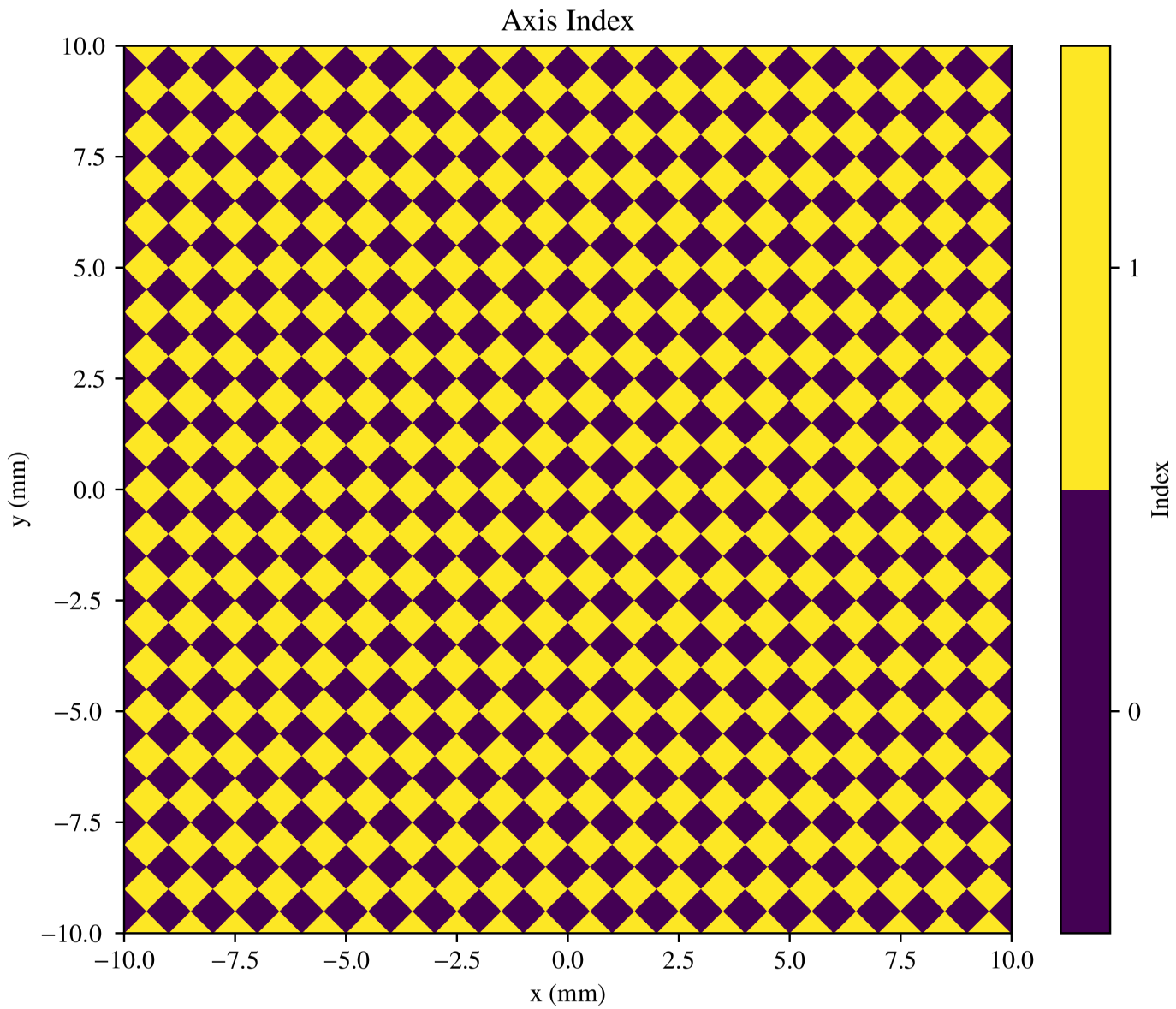

Figure 5: The axis-index of coordinates on an example anode with 1 mm wide pads. Strips of pads indexed "0" run along y and discriminate along x (x-strips), while those indexed "1" run along x and discriminate along y (y-strips).

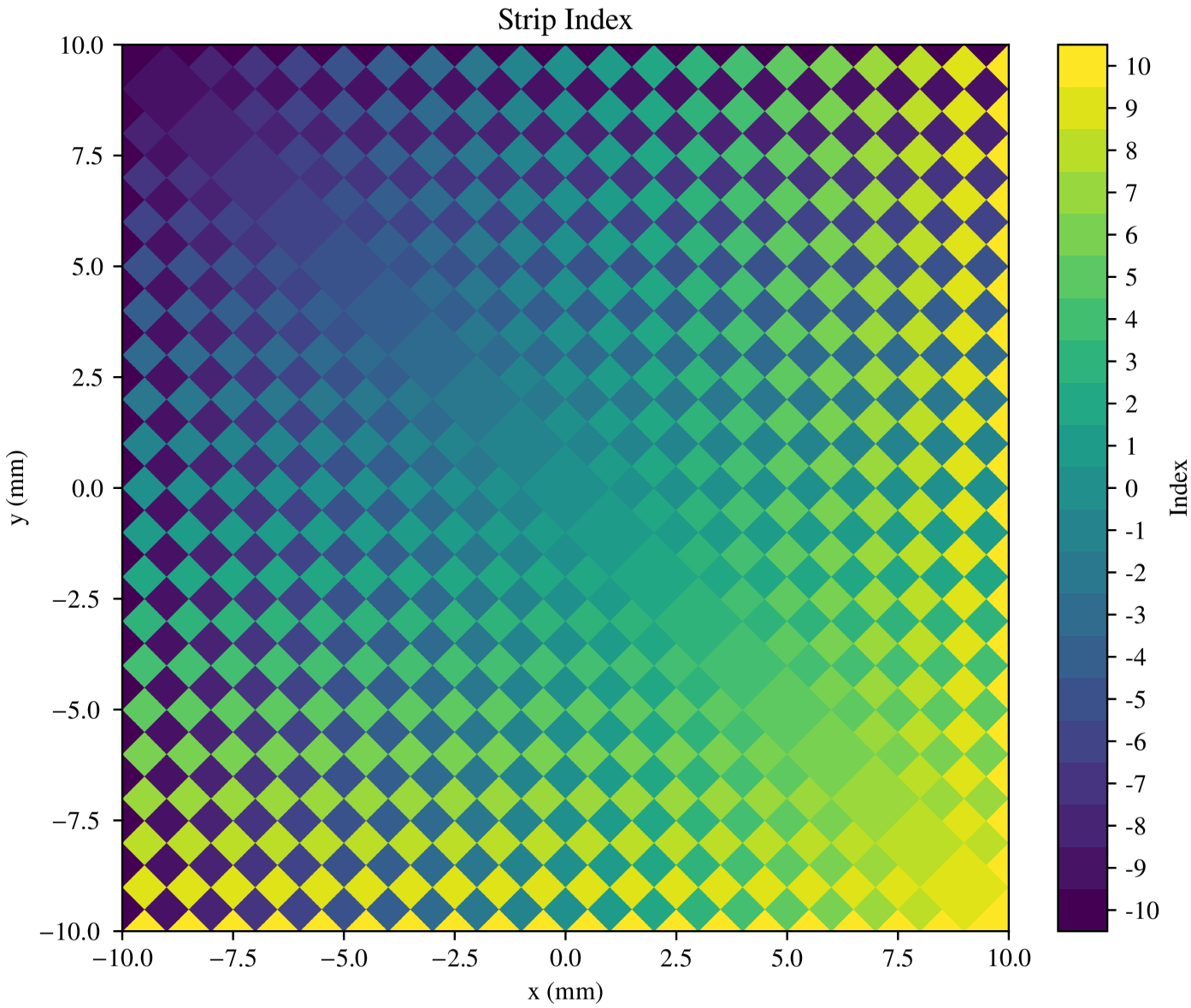

Figure 6: The strip-index of coordinates on an example anode with 1 mm wide pads. Each small square is a single pad, with the larger squares along the diagonal being groups of four pads where orthogonal strips of like strip-index intersect, where strips can be identified as horizontal or vertical runs of constant value.

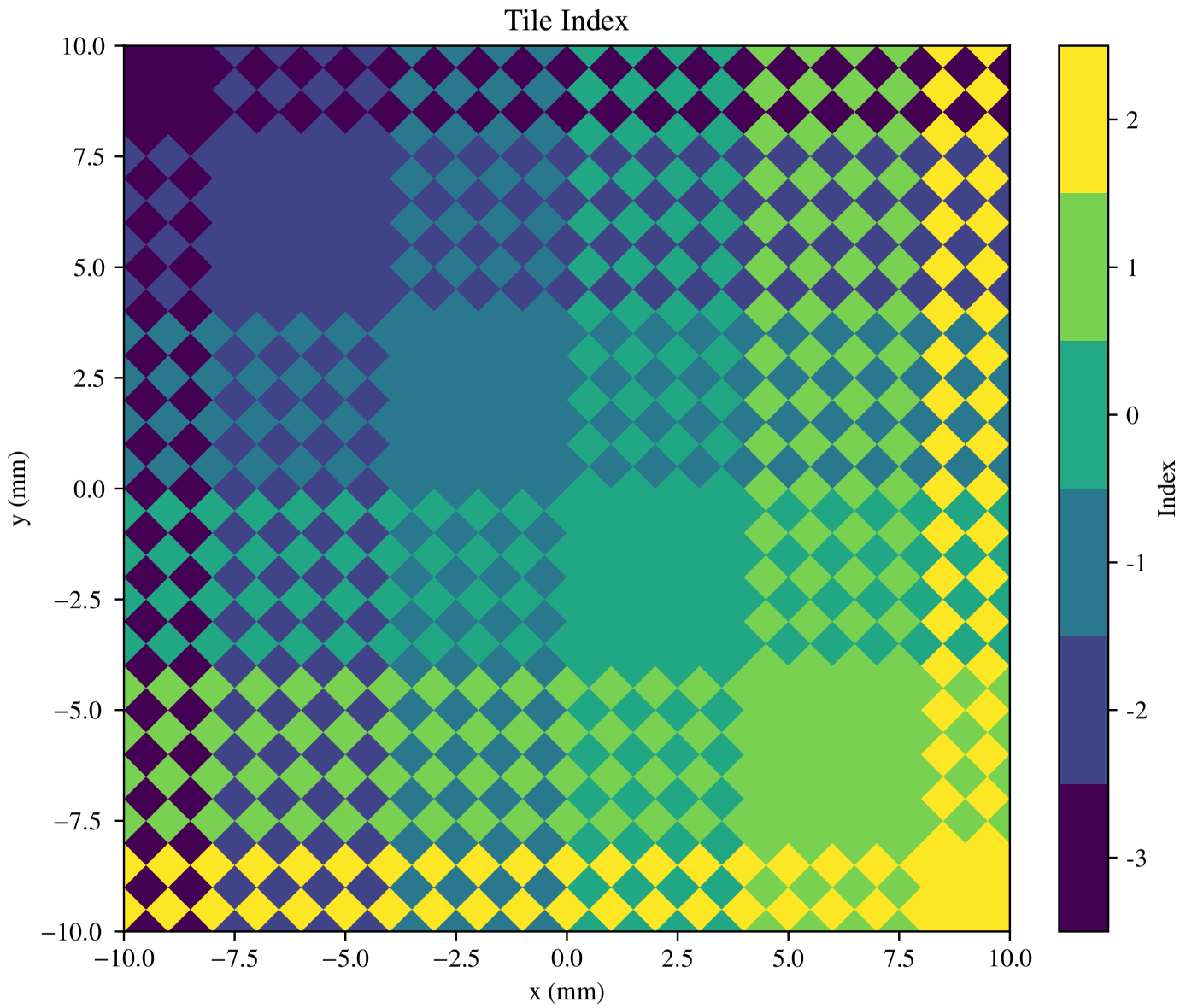

Figure 7: The tile-index of coordinates on an example anode with 1 mm wide pads and 4 pads per strip. Strips are split into segments and indexed along their length, producing “strips of strips”.

In a much simpler process, the time-sample index is produced through the flooring of a single operation:

$$t_{index} = \lfloor tf \rfloor \tag{16}$$

where t is the time of arrival and f is the time-sampling frequency, which is the inverse of the time-sample width.

Finally, the fragments must be sorted and aggregated by unique index, such that any one strip in a tile has only one energy value per time-sample. This step was originally performed using Python's dictionary objects, using index tuples as keys, however this was both inefficient and not vectorizable. Instead, the current solution has been to use the SciPy Stack's *Pandas* library, which allows NumPy arrays to be converted into indexed database-like data structures, with versatile sorting methods implemented in C.

This initial aggregation, including time, is intended to represent the final distribution of the charge upon arrival at the anode. However, the surface charges formed in response to the drifting charge will prevent direct detection of this collection in a real detector, as the drifting electrons are captured and neutralized immediately on contact with the anode (with excess surface charge in adjacent elements dissipating as the drifting charge's fields become perpendicular). Instead, the build-up (and dissipation) of the surface charge is measurable as current into (and out of) the anode, and this *current waveform* may be integrated to find the cumulative charge collected by the anode. Therefore, to produce the cumulative charge-equivalent energy collected by each strip during the event, the time-collection bins (time-samples over strips) are further summed across the time axis.

Collection noise, representing the cumulative effects of noise in the current waveform, is implemented in the form of a Gaussian signal deviation on every strip:

$$E' = E + n\sigma \tag{17}$$

where E is the unaltered cumulative energy detected by an arbitrary strip, σ is the standard deviation of the noise, n is a random normal deviate, and E' is the final energy detected. A threshold filter then excludes any strips which have, after noise, collected less charge than a given minimum, typically about 4.5 times the standard deviation of the noise, to exclude noise-only signals far from the site of collection. Since the fragmentation algorithm never calculates noise on strips that have not collected a charge fragment, this is necessary to produce sensible results.

However, the fragmentation algorithm, when used with sufficiently large fragment sizes to be practical (a few thousand fragments per event), will also inherently generate an unrealistic form of noise from its coarse distribution. An example of this can be seen in Figure 8. Producing a finer distribution by this method requires a smaller fragment size, which greatly increases computational time through inversely increasing the number of fragments.

The expected granularity of a physical cloud of electrons is much finer, with about 100 000 electrons per event (2.5 MeV of deposited energy at approximately 25 eV per electron). This suggests that an analytic approach, calculating the distribution at an infinitely fine granularity, would be much more efficient. Further, the number of energy deposits for a typical event is usually within a few dozen, and we can see from Figure 8 that, near the maximum drift length of 1.27 m, each deposit itself affects at most a handful of strips across several time slices. Only about a hundred pad/time-slice cells are needed to calculate the distribution for a maximally-distant deposit, and much fewer for nearer ones. This restricts the total number of calculated elements to at worst a couple thousand per event, which is the same order of magnitude or better than the fragmenta-

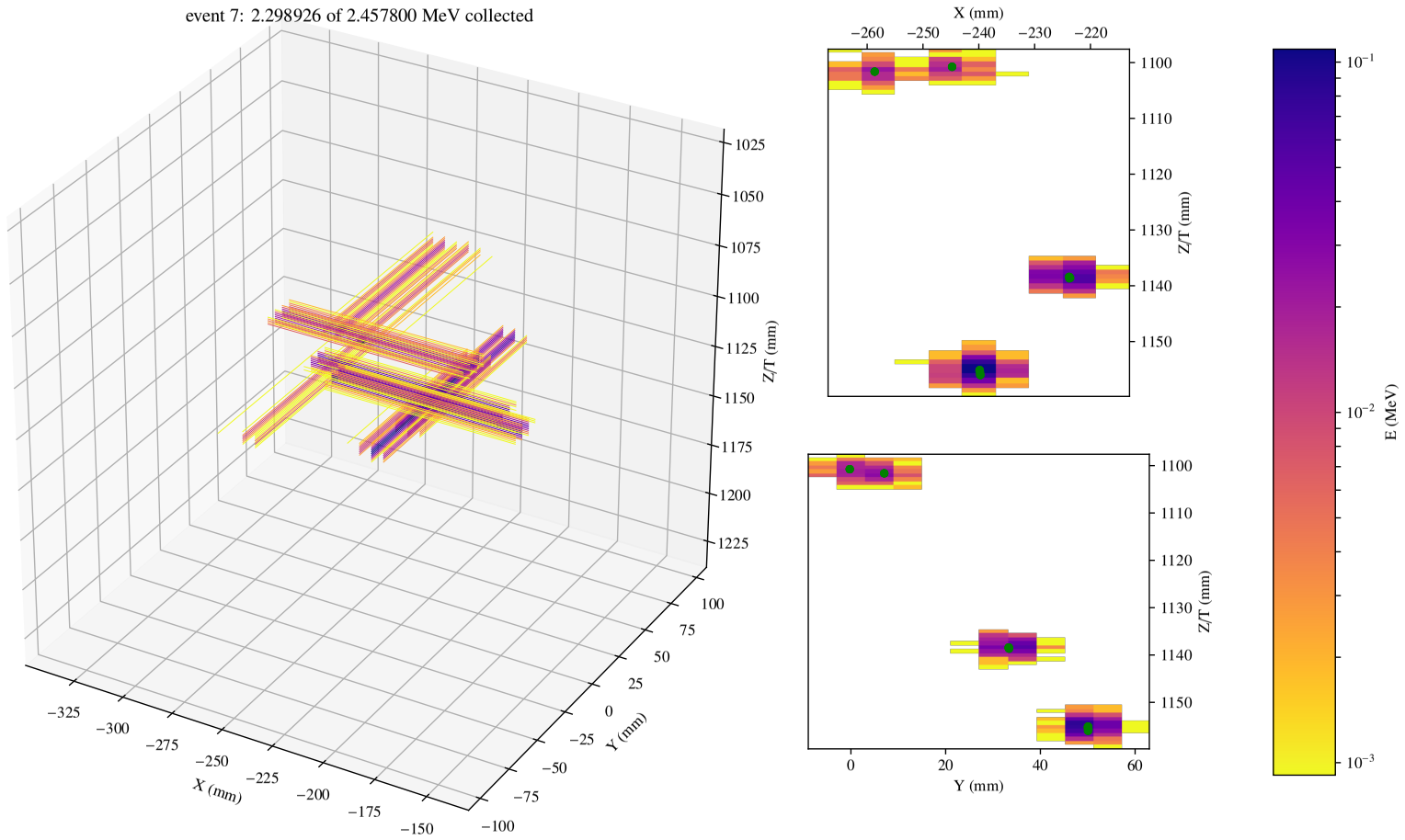

Figure 8: An example rendering of the output of the fragmentation algorithm on deposits (marked in green) from a 2.4578 MeV γ-ray, using a fragmentation size of 1 keV. All other parameters are in Table 2 (see Section 4). The collection over time of the x and y strips is shown at the top and bottom right, respectively, while the figure on the left shows a three-dimensional combination of these, including the spans of the strips as line-segments. Note the uneven fringes, in comparison with Figure 9.

tion algorithm, but without the sacrifice to granularity. To take advantage of this, the Gaussian integration algorithm was implemented (Section 3).

3 Gaussian Algorithm

A more efficient alternative to the fragmentation algorithm is to treat diffusion analytically. By integrating the probability density across element boundaries, the electron cloud is handled with the finest degree of granularity at minimal computational cost.

3.1 Diffusion

3.1.1 Integration

The diffusion equation in one dimension, for a constant diffusion coefficient D, is:

$$\frac{\partial \phi(x,t)}{\partial t} = D\frac{\partial^2 \phi(x,t)}{\partial x^2} \tag{18}$$

where ϕ is the density distribution of diffusion along x. A known solution to this differential equation is:

$$\phi(x,t) = \frac{1}{\sqrt{4\pi D t}} \exp\left(\frac{-(x-x_0)^2}{4Dt}\right) \tag{19}$$

which is a normal Gaussian of standard deviation $\sigma = \sqrt{2Dt}$, and is also the probability density function for a random walk, a model for diffusion, as is used in Section 2. At $t = 0$, the Gaussian reduces to a Dirac delta distribution, a point source from which diffusion begins:

$$\phi(x,0) = \delta(x_0) \tag{20}$$

The isotropic n-dimensional case of this is similar; using two-dimensions as an example:

$$\frac{\partial \phi(x,y,t)}{\partial t} = D\nabla^2 \phi(x,y,t) \tag{21}$$

$$\begin{aligned} \phi(x,y,t) &= \frac{1}{4\pi Dt}\, \exp\left(\frac{-(x-x_0)^2-(y-y_0)^2}{4Dt}\right) \\ &= \prod_{w\in\{x,y\}} \frac{1}{\sqrt{4\pi Dt}}\, \exp\left(\frac{-(w-w_0)^2}{4Dt}\right) \end{aligned} \tag{22}$$

$$\phi(x,y,0) = \delta(x_0)\delta(y_0) \tag{23}$$

which is the product of a normal Gaussian in x with one in y, each of which independently obeys Equation 18, along the respective axis.

The cumulative distribution function of a normal Gaussian can be expressed using the antisymmetric *error function* (erf):

$$\operatorname{erf}(x) = \frac{1}{\sqrt{\pi}} \int_{-x}^{+x} e^{-x'^2} dx' = \frac{2}{\sqrt{\pi}} \int_0^x e^{-x'^2} dx' \tag{24}$$

$$\operatorname{erf}(\infty) = 1 = -\operatorname{erf}(-\infty) \tag{25}$$

Therefore, the cumulative distribution $\Phi(x)$ of the density $\phi(x)$ becomes:

$$\begin{aligned} \Phi(x) &= \int_{-\infty}^{x} \phi(x')\, dx' = \int_{-\infty}^{x} \frac{e^{\frac{-(x'-x_0)^2}{2\sigma^2}}}{\sqrt{2\pi\sigma^2}}\, dx' \\ &= \frac{1}{\sqrt{\pi}} \int_{-\infty}^{\left(\frac{x-x_0}{\sqrt{2}\sigma}\right)} e^{-\left(\frac{x'-x_0}{\sqrt{2}\sigma}\right)^2} d\left(\frac{x'-x_0}{\sqrt{2}\sigma}\right) \\ &= \frac{1}{2}\left(\operatorname{erf}\left(\frac{x-x_0}{\sqrt{2}\sigma}\right)+1\right) \end{aligned} \tag{26}$$

If inverted, this gives us a transformation from a uniformly distributed $u = \Phi(x)$ to a normally distributed $g = x$ with mean $\mu = x_0$:

$$g = \sigma\sqrt{2}\,\mathrm{erf}^{-1}(2u - 1) + \mu = \sigma n + \mu \tag{27}$$

which, as expected, allows any normal distribution to be sampled from the standard normal distribution n ($\sigma = 1$ and $\mu = 0$) by scaling and shifting, as used in Section 2.1. (Incidentally, performing this inversion with the more easily integrated polar representation of a two-dimensional Gaussian yields the Box-Muller transform and Marsaglia polar method, related and commonly used methods of deriving normally distributed random values from uniformly distributed values, two at a time.)

Finally, in the case of diffusion, we have $\sigma = \sqrt{2Dt}$, therefore:

$$\Phi(x, t) = \frac{1}{2}\left(\mathrm{erf}\left(\frac{x - x_0}{\sqrt{4Dt}}\right) + 1\right) \tag{28}$$

$$g = \sqrt{2Dt}\,n + \mu \tag{29}$$

where the latter is a restatement of Equation 2 from the fragmentation algorithm, and the former is the cumulative distribution function needed to analytically calculate the portion of a diffusion cloud that lies between two boundaries along any one dimension.

3.1.2 TPC

Diffusion of drifting electrons in the TPC can be modelled as a drifting three-dimensional anisotropic Gaussian with the probability density function (normalized in x, y, and z):

$$P(x, y, z, t) = \frac{1}{8\pi^{\frac{3}{2}} D_t D_l^{\frac{1}{2}} t^{\frac{3}{2}}} \exp\left(-\frac{(x - x_0)^2 + (y - y_0)^2}{4D_t t} - \frac{(z - (z_0 - v_d t))^2}{4D_l t}\right) \tag{30}$$

$$Q(x, y, z, t) = Q_{total} P(x, y, z, t) \tag{31}$$

where D_t is the transverse diffusion coefficient, D_l is the longitudinal diffusion coefficient, v_d is the drift speed, and drift occurs along the z axis towards the xy plane (the anode). The density of charge (or equivalent energy) Q is the probability density P modified to an amplitude of Q_{total}, the total charge.

A corresponding cumulative distribution H_V at any given time t over a volume V can be derived as

$$\begin{aligned} H_V &= \iiint_V dV\, P(x,y,z,t) = \iiint_V dV\, \frac{e^{-\frac{(x-x_0)^2+(y-y_0)^2}{4D_t t} - \frac{(z-(z_0-v_d t))^2}{4D_l t}}}{8\pi^{\frac{3}{2}} D_t D_l^{\frac{1}{2}} t^{\frac{3}{2}}} \\ &= \frac{1}{8}\left(\operatorname{erf}\left(\frac{z-(z_0-v_d t)}{\sqrt{4D_l t}}\right)+1\right) \prod_{w\in\{x,y\}} \left(\operatorname{erf}\left(\frac{w-w_0}{\sqrt{4D_t t}}\right)+1\right)\Bigg|_V \\ Q_V &= Q_{total} H_V \end{aligned} \tag{32}$$

where $dV = dx\,dy\,dz$, and Q_V is the total charge contained in V.

If, instead, we take $z = 0$ (the anode) and we integrate over time ($dV_t = dx\,dy\,v_d dt$), to acquire the charge (Q_{V_t}) collected by a single square pad on the anode during that time, we have

$$H_{V_t} = \iiint_{V_t} dV_t\, P(x,y,0,t) = \iiint_{V_t} dV_t\, \frac{e^{-\frac{(x-x_0)^2+(y-y_0)^2}{4D_t t} - \frac{(z_0-v_d t)^2}{4D_l t}}}{8\pi^{\frac{3}{2}} D_t D_l^{\frac{1}{2}} t^{\frac{3}{2}}} \tag{33}$$

$$Q_{V_t} = Q_{total} H_{V_t} \tag{34}$$

which is difficult to integrate [35]. (Note, however, that it is now normalized over t instead of z, due to the charge-drift term $v_d t$; this is further borne out in the change from dz to $v_d dt$.) Therefore, we will approximate the shape of the diffusion cloud as if it were arriving simultaneously with its

center, at time $t_0 = z_0/v_d$:

$$\begin{aligned} H_{V_t} &\approx \iiint_{V_t} dV_t\, P'(x,y,t) = \iiint_{V_t} dx\, dy\, dt\, \frac{e^{-\frac{(x-x_0)^2+(y-y_0)^2}{4D_t t_0} - \frac{(t-t_0)^2}{4(D_l/{v_d}^2)t_0}}}{8\pi^{\frac{3}{2}} D_t (D_l/{v_d}^2)^{\frac{1}{2}} {t_0}^{\frac{3}{2}}} \\ &= \frac{1}{8}\left(\operatorname{erf}\left(\frac{t-t_0}{\sqrt{4(D_l/{v_d}^2)t_0}}\right)+1\right) \prod_{w\in\{x,y\}} \left(\operatorname{erf}\left(\frac{w-w_0}{\sqrt{4D_t t_0}}\right)+1\right)\Bigg|_{V_t} \end{aligned} \tag{35}$$

which is again a product of three error function difference evaluations. Similarly to the time-approximation for the fragmentation algorithm (Equation 5, Section 2.1), this is a substitution of $\sigma = \sqrt{2Dt}$ with $\sigma = \sqrt{2Dt_0}$ along every axis. As shown in Section 2.1 by Equation 6, using realistic parameters from Table 2, the longitudinal representation is valid for a detector of this size under typical drift conditions. The transverse axes are minimally changed, as the same conditions ensure that the variation in σ along these axes is small across the bulk of the distribution.

In the case of impurities capturing electrons and attenuating the signal, the charge density function has an additional (unnormalized) exponential factor:

$$Q_\lambda = e^{-\frac{t}{\lambda}} Q_{total} P \tag{36}$$

with mean electron lifetime λ. Incorporating this factor into the z component of P, as a one-dimensional Gaussian in the anode-time approximation P', the combined exponents can be written as a quadratic equation and rearranged:

$$\ln\left(\sqrt{2\pi{\sigma_l}^2}g(t)\right) = -\frac{(t-t_0)^2}{2{\sigma_l}^2} \tag{37}$$

$$\begin{aligned} \ln\left(\sqrt{2\pi{\sigma_l}^2}g_\lambda(t)\right) &= -\frac{(t-t_0)^2}{2{\sigma_l}^2} - \frac{t}{\lambda} \\ &= -\frac{\left(t-(t_0-\frac{{\sigma_l}^2}{\lambda})\right)^2}{2{\sigma_l}^2} - \frac{t_0-\frac{{\sigma_l}^2}{2\lambda}}{\lambda} \end{aligned} \tag{38}$$

This is a Gaussian with a shifted mean and diminished amplitude, where $g(t)$ is a normalized Gaussian in t with (longitudinal) standard deviation σ_l, and $g_\lambda(t) = g(t)\, e^{-t/\lambda}$. The attenuated distribution can therefore also be produced by Equation 35 after adjusting the mean and total amplitude appropriately:

$$Q_\lambda(x, y, 0, t) \approx e^{-\frac{t}{\lambda}} Q_{total} P'(x, y, t) = \left(e^{-\frac{t_0 - \frac{\sigma_l^2}{2\lambda}}{\lambda}} Q_{total} \right) P'\left(x, y, \left(t + \frac{\sigma_l^2}{\lambda}\right)\right) \tag{39}$$

(where $\sigma_l{}^2 = 2(D_l / v_d{}^2) t_0$) which is trivial to accommodate during integration.

3.2 Anode

In the Gaussian algorithm, diffusion is calculated directly on the grid of the anode's pads. Prior to this, the means, variances, and amplitudes for each deposit are calculated from position and attenuation. Similarly to the fragmentation algorithm (see Section 2.2), the xy mean μ of each Gaussian distribution is subjected to rotation and scaling:

$$\mu = x_0 + y_0 i \tag{40}$$

$$\begin{aligned} \mu_p &= (x_0 + y_0 i) \frac{(1 + i)}{\sqrt{2}} \frac{\sqrt{2}}{w_p} \\ &= \frac{(x_0 - y_0) + (x_0 + y_0) i}{w_p} \\ &= x_{0_p} + y_{0_p} i \end{aligned} \tag{41}$$

where w_p is again the diagonal width of the pads, while x_{0_p} and y_{0_p} are the scaled (and rotated) means in the xy-plane. This scales the rotated coordinate system such that the pads and their boundaries are integer units. Time is also scaled to the time-sampling intervals:

$$t_{0_p} = t_0 f = z_0 \frac{f}{v_d} \tag{42}$$

where f is the time sampling frequency, the inverse of the time-sample width. The variances (*transverse* σ_t and *longitudinal* σ_l) are similarly scaled:

$$\sigma_t{}^2 = 2D_t t_0 \tag{43}$$

$$\sigma_{t_p}{}^2 = \sigma_t{}^2 \frac{2}{w_p{}^2} \tag{44}$$

$$\sigma_l{}^2 = 2(D_l / v_d{}^2) t_0 \tag{45}$$

$$\sigma_{l_p}{}^2 = \sigma_l{}^2 f^2 \tag{46}$$

With the parameters scaled onto an integer coordinate system, the distributions for each axis can be produced using integer arrays of pad boundaries to evaluate the adjusted error-functions. Since these idealized distributions are infinite in nature, a cutoff width needs to be chosen. This width is user-defined and chosen in units of standard deviations, ideally with a value of at least 3σ. Along each axis, the width of the calculated distribution is the smallest number of pads that is guaranteed to contain the designated width of the distribution within. To maintain vectorization within the algorithm, this width is calculated for the widest distribution only (ultimately the deposit furthest from the anode) and in ignorance of the position of the mean within the central cell, then applied to every deposit in the event. As such, every distribution will, in both intermediary and final forms, have the same shape in memory, and can be stored in arrays.

Using the arrays of boundaries, the three components of Equation 35 are used to generate three one-dimensional independent Gaussian distributions across the pad-time cells. These three arrays of bins are then multiplied together in a three-way outer-product to produce the final three-dimensional distribution, each cell corresponding to one instance of V_t (Equation 35). These are further multiplied by the intended amplitude of the distribution (the deposit's charge or energy value Q_{total}), producing the desired relative contribution to each cell for each deposit.

To acquire the indices for each cell, the lower bounds of each cell are used as the integer pad coordinates from Equation 10, from which the de-rotation is followed to create arrays of indices

for each cell in each distribution. These are then aggregated and summed by index, with Gaussian noise and threshold applied to the cumulative collection for each strip over time, as with the fragmentation algorithm.

In contrast to the fragmentation algorithm, the Gaussian integration algorithm produces distributions with smooth edges (as seen in Figure 9). This divorces the macroscopic electron distribution from uncontrolled noise-like effects, restricting noise to explicitly given values.

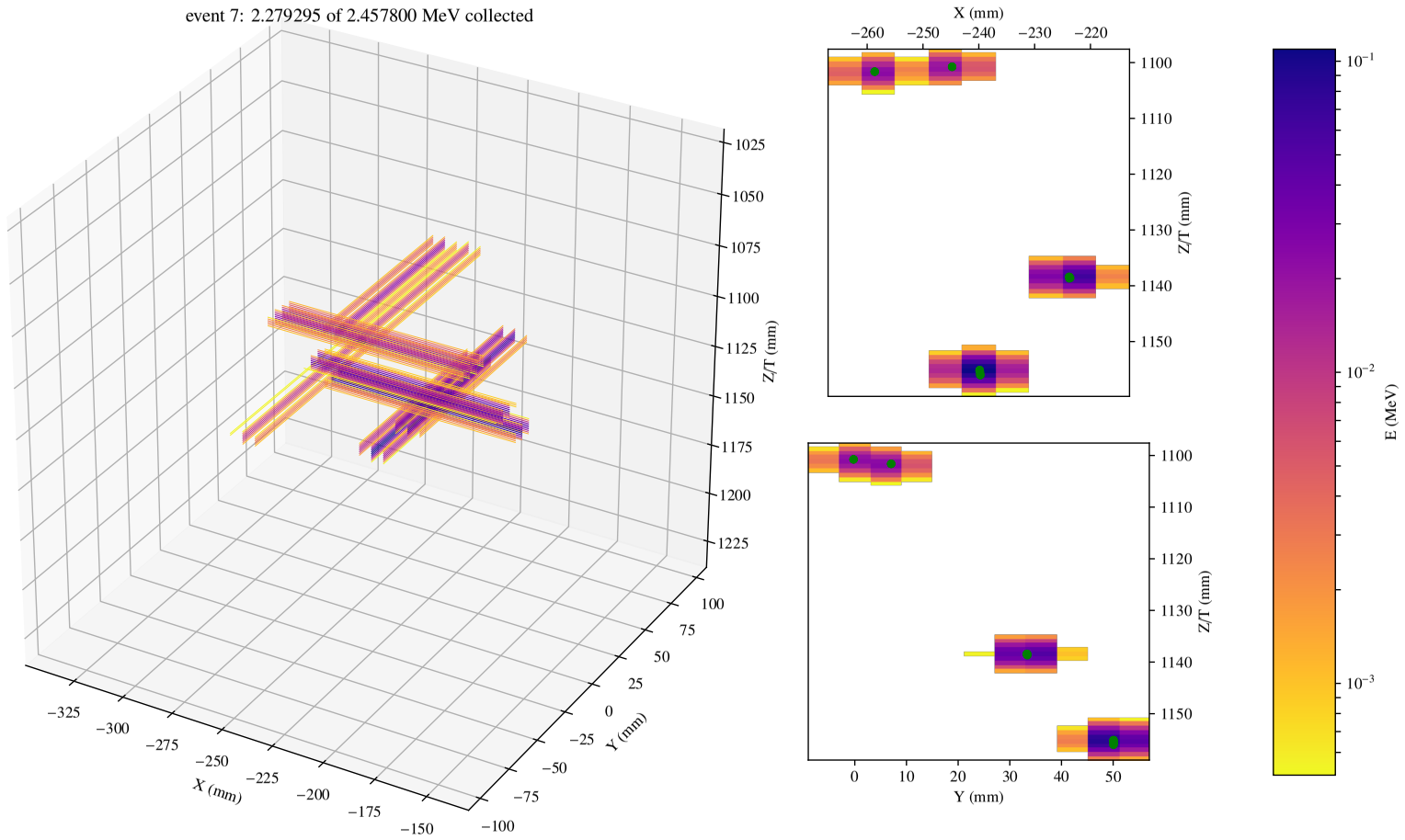

Figure 9: An example rendering of the Gaussian integration algorithm on deposits (marked in green) from a 2.4578 MeV γ-ray, over an integration width of 4σ and masking volume-elements below 0.5 keV. All other parameters are in Table 2 (see Section 4). The collection over time of the x and y strips is shown at the top and bottom right, respectively, while the figure on the left shows a three-dimensional combination of these, including the spans of the strips as line-segments. Note the smooth fringes, in comparison with Figure 8.

4 Validation

4.1 Readout Distribution

The first set of validation simulations was performed with the parameters indicated in Table 2, or modifications thereof, primarily on deposits generated uniformly throughout the TPC volume. A set of 1 million events for each of $2\nu\beta\beta$ in ^{136}Xe, the equivalent $0\nu\beta\beta$, and 2.4578 MeV γ-rays were generated in by the `nEXO_MC` Geant4 application, such that all three types of event have the same total energy of 2.4578 MeV (including the escaping neutrinos in $2\nu\beta\beta$).

In Figures 10-15 we can see the distributions of the charge readout across all events, relative to the distributions of the deposits, as well as the energy spectra of each event type. We can see that the

Initial Test Parameters

Drift Parameters		Anode Parameters	
Trans. Diffusion	$0.0055\,\mathrm{mm^2\,\mu s^{-1}}$	Pad Width	6 mm
Long. Diffusion	$0.0013\,\mathrm{mm^2\,\mu s^{-1}}$	Strip Length	16 Pads
Drift Velocity	$1.705\,\mathrm{mm\,\mu s^{-1}}$	Sampling Rate	2 MHz
Purity	10 ms	Threshold	4.74 keV
Other Parameters			
Event Distribution	uniform in TPC	`readout` Algorithm	Gaussian
Event Energy	2.4578 eV	Events Processed (`readout`)	1 000 000

Table 2: The initial set of parameters with which validation tests of the `readout` package were performed, unless otherwise indicated. This set of parameters was intended to be largely realistic: drift velocity and transverse diffusion were taken from [35], while longitudinal diffusion was estimated from [36], from an assumed drift field of $380\,\mathrm{V\,cm^{-1}}$. The threshold is 300 electrons at 15.8 eV per electron, approximately the w-value of xenon [33]. Events were generated in a uniformly in the TPC.

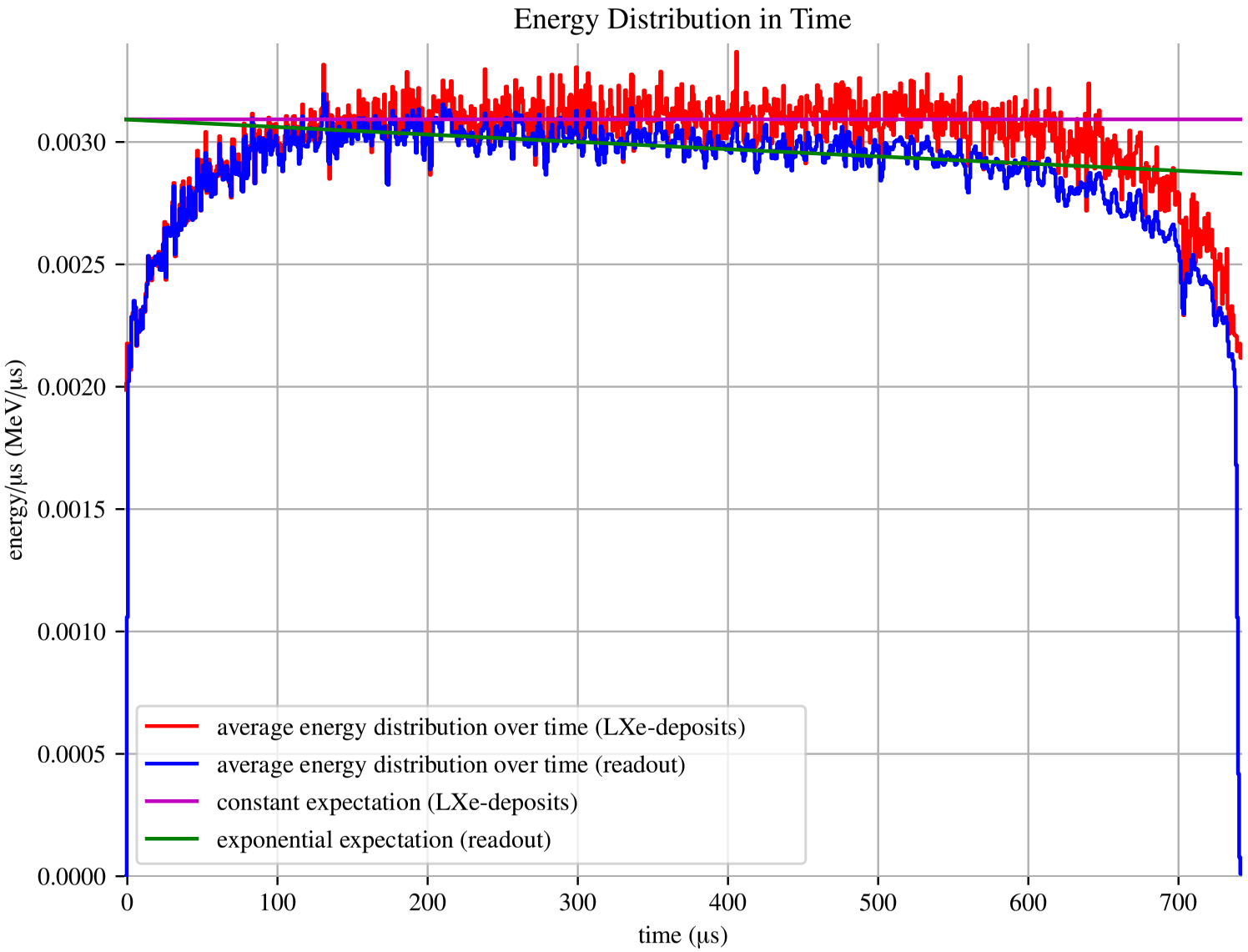

Figure 10: The distribution of energy in time of 1 million 2.4578 MeV γ events uniformly distributed in the TPC. Note that the 739 μs boundary denotes the location of the cathode, 1.26 m from the anode with a drift speed of 1.705 mm μs^{-1}. The input deposits continue into the narrow space behind the cathode.

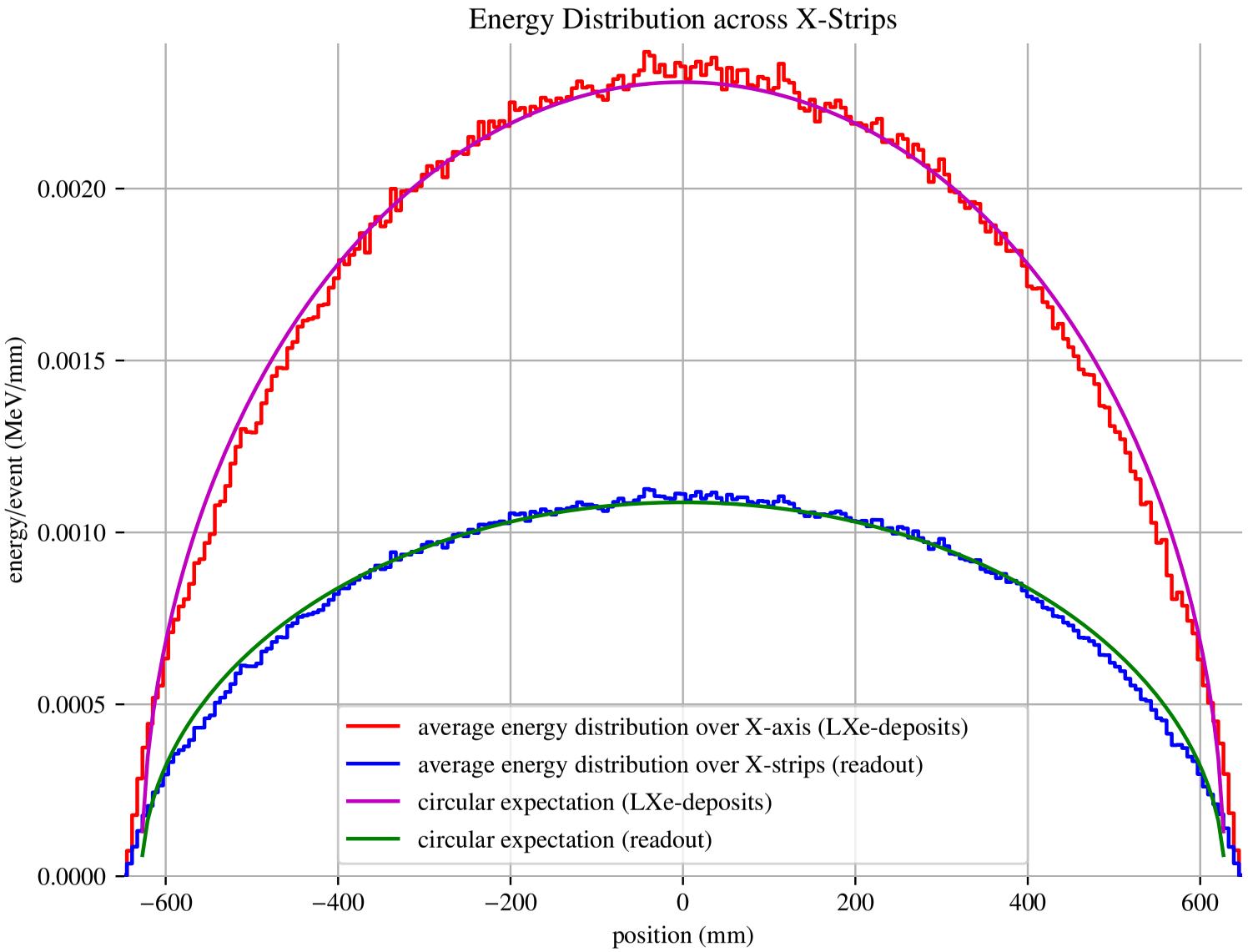

Figure 11: The distribution of energy across x-strips of 1 million 2.4578 MeV γ events uniformly distributed in the TPC. Note that every deposit has been plotted, while only half of the readout on the anode has been plotted, resulting in a factor of two. The plot for y-strips is similar, containing the other half of the readout.

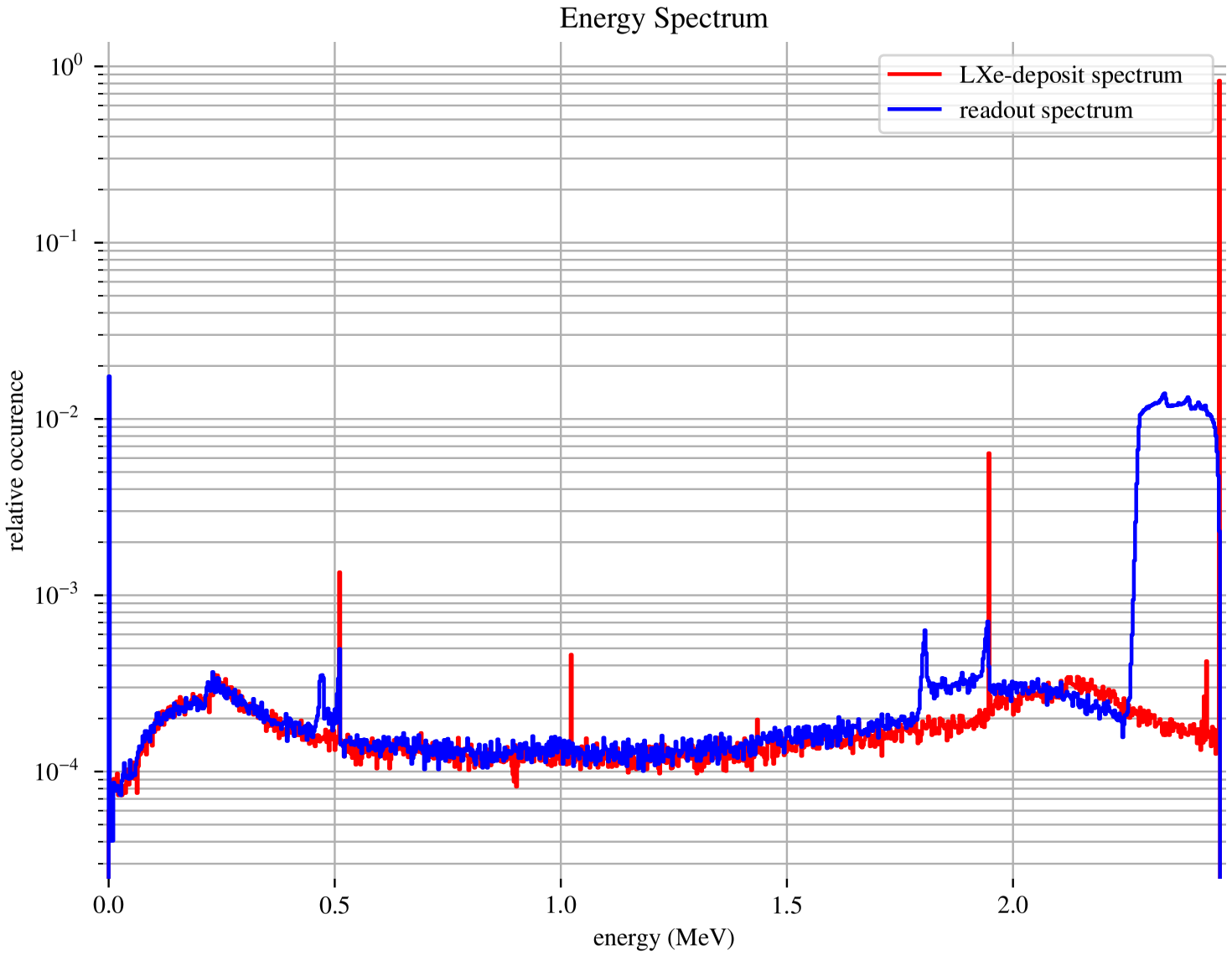

Figure 12: The energy spectrum of 1 million 2.4578 MeV γ events uniformly distributed in the TPC. Note the multiple escape and back-scatter peaks, several of which are represented in the readout. The full-energy peak is smeared in two parts: a plateau with a width 7.1% of the maximum energy due to attenuation across the TPC length, and a slight tail caused by the threshold filter. Due to the low threshold-smearing, the single-escape and single-back-scatter peaks are visibly split by their distributions, as in Figure 17.

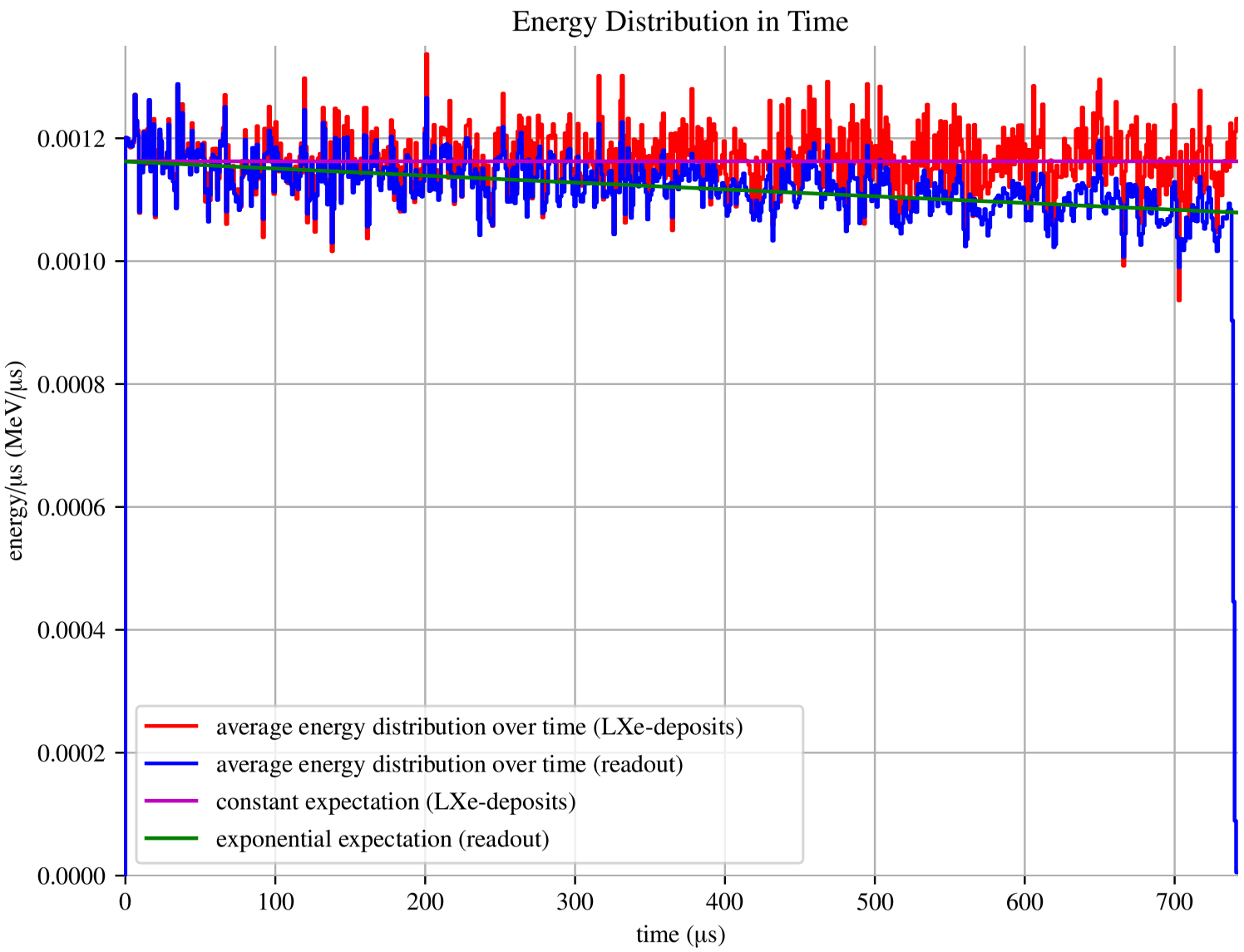

Figure 13: The distribution of energy in time of 1 million ^{136}Xe 2νββ events uniformly distributed in the TPC. This is similar to Figure 10, with less drop-off near the edges, due to the shorter track-length of β-events. The 0νββ distribution is similar.

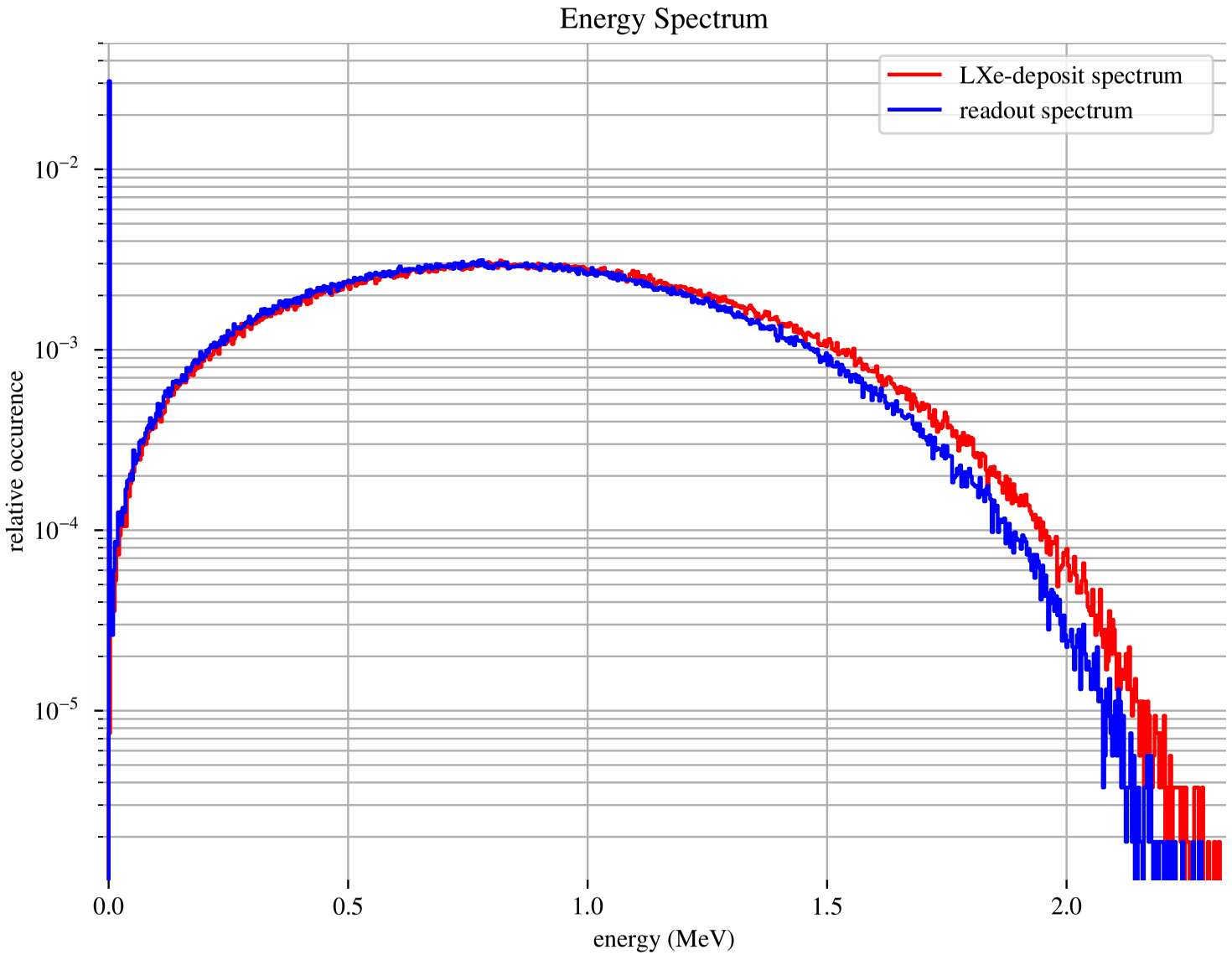

Figure 14: The energy spectrum of 1 million ^{136}Xe 2νββ events uniformly distributed in the TPC.

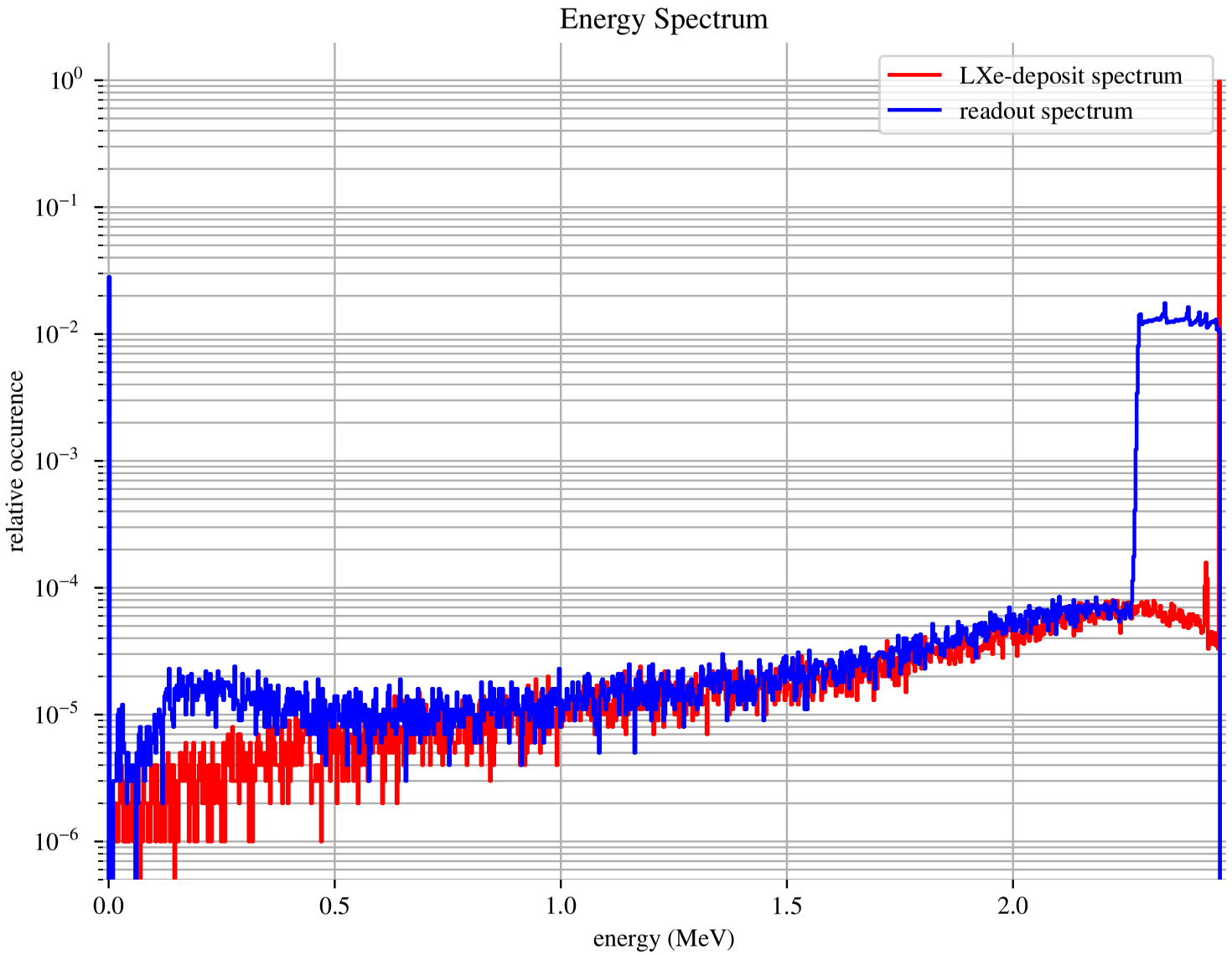

Figure 15: The energy spectrum of 1 million ^{136}Xe 0νββ events uniformly distributed in the TPC. The full-energy plateau represents a 7.1% maximum attenuation in energy, as in Figure 12. The plateau is sharper due to the shorter track-length limiting escapes near the anode and cathode. This is similar to the sharpness in the time distribution of ββ events (14).

distributions of the readout in space and time follow those of the originating deposits closely. We can also see from the distributions along the time axis that the readout has an exponential decay relative to the deposits; since the threshold filter is not applied to the time-distribution output, and only to the time-cumulative output, this decay is entirely unaltered from its expected value.

The energy spectra show more nuanced details, however. Due to its more elaborate structure, the spectrum of the γ rays is the most useful in demonstrating these. Figure 12 shows the readout energy spectrum for the base parameters. The full-energy peak becomes smeared across a plateau with a width of 7.1 % of the maximum energy value (2.4578 MeV), which corresponds to the attenuation from a 10 ms purity (mean-lifetime) across a 1.2605 m long TPC. Each peak of deposited energy produces an image in collection representing that peak's distribution in the TPC; for example, the single-escape peak (at 1.9468 MeV) is primarily found near the TPC's walls, where a single 511 keV positron-annihilation photon may easily escape (hence the name), and so produces two peaks, one for either end of the TPC, and a shallow bowl for the axial wall. By contrast, the full energy peak shows a relatively uniform plateau, representing a uniform distribution in the TPC volume, which is large enough to prevent most γ-rays and scattered electrons from escaping. There is a small additional tail of smearing on each peak caused by diffusion and attenuation bringing the signal on certain strips in certain events below the threshold, however, with the low threshold level in this example, it is negligible.

We can increase the attenuation and the threshold filter (Figure 16) to exaggerate both the full-energy peak's plateau and its tail. With a purity of 1 ms, the plateau is expanded to 52 % of the maximum energy. This is further smeared by an increase by a factor of ten in the threshold, and the pad size being reduced to 3 mm halving the amount of energy landing on any given strip, and thus effectively further doubling the strength of the threshold. With a total increase in threshold strength by a factor of 20, the tail becomes very apparent.

Similarly, if diffusion and the threshold are disabled (Figure 17), the tail disappears completely on the main peak and others, instead revealing sharper images for each of the peaks. We can

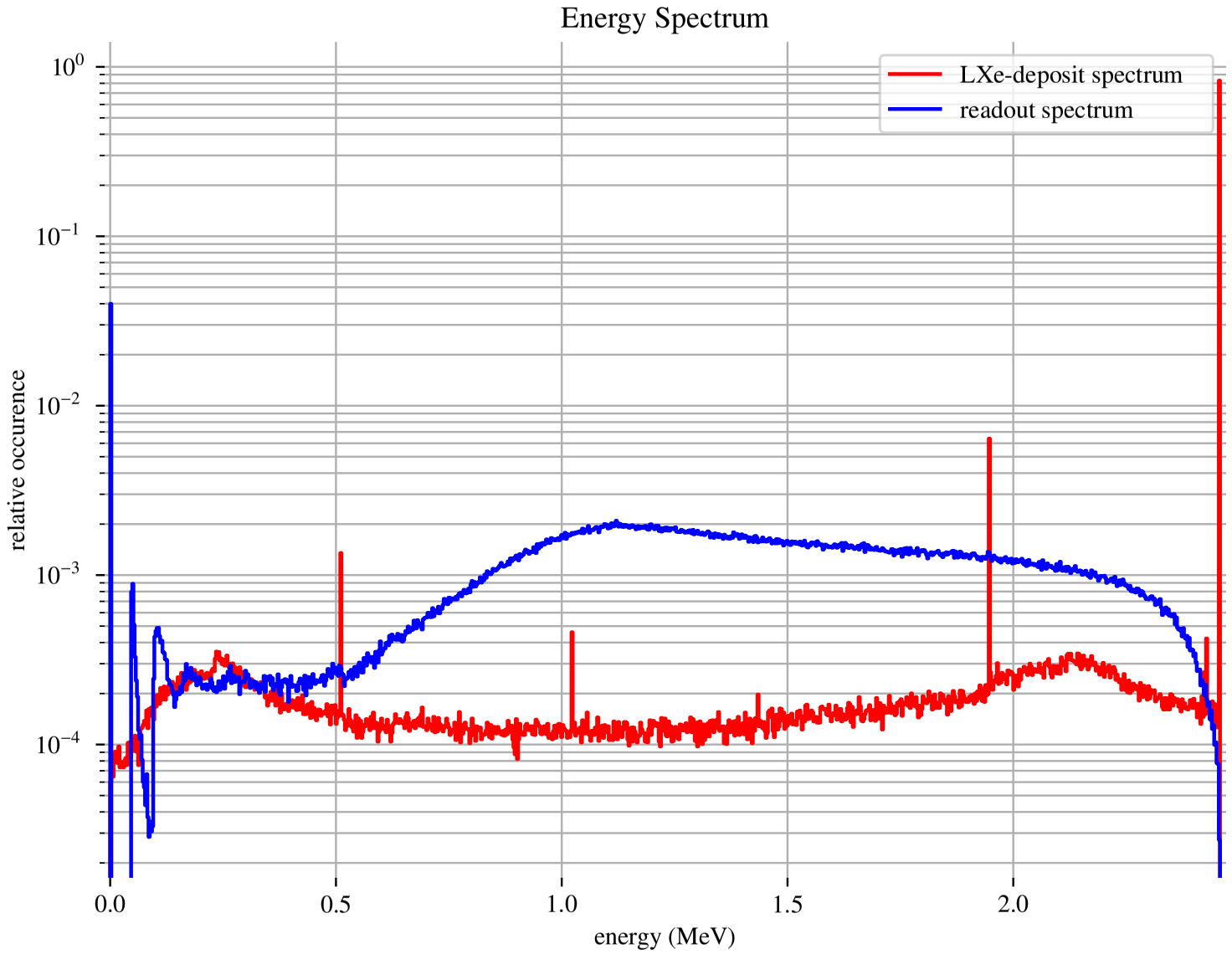

Figure 16: The energy spectrum of 1 million 2.4578 MeV γ events uniformly distributed in the TPC, with a purity of 1 ms, a threshold of 47.4 keV, and 3 mm pads (32 pads per strip). The full-energy peak's plateau has been widened to 52%, with further smearing by the ten-fold increase in the threshold working in synergy with the halved areas of the strips. The effects of the threshold are clearly visible in the low-energy region, with the complete exclusion of events with deposited energies below the threshold value.

also further disable attenuation (or set purity to an infinite value), to reveal a near duplicate of the original spectrum (Figure 18).

4.2 Comparison with Detailed Simulation

A more detailed simulation exists with which the `readout` module may be compared, as briefly described in Section 1.5. This simulation, through the simulation of currents building and dissipating induced surface charges, records the cumulative charge collected on each strip over time. The current waveform has electronics noise, from which a standard deviation for the cumulative collection noise is produced. As such, the comparable values from the `readout` package are those for cumulative collection over time, as described in Section 2.2.

To facilitate comparison, a reconstruction variable, with potential to be used for discrimination between β and γ events, was chosen [26, 37]. The *average distance to the reconstructed center*, d_r, is calculated as follows:

$$\bar{x} = \frac{\sum\limits_x xE_x}{\sum\limits_x E_x} \qquad \bar{y} = \frac{\sum\limits_y yE_y}{\sum\limits_y E_y} \tag{47}$$

$$d_x = \frac{\sum\limits_x |x - \bar{x}|E_x}{\sum\limits_x E_x} \qquad d_y = \frac{\sum\limits_y |y - \bar{y}|E_y}{\sum\limits_y E_y} \tag{48}$$

$$d_r = \sqrt{{d_x}^2 + {d_y}^2} \tag{49}$$

where $\bar{x}$, the *reconstructed center* along x, is the center of charge (or equivalent energy E_x) across all x-strips, for one event, with a similar $\bar{y}$ existing for y-strips. d_x and d_y are the average distance (absolute deviation) of x and y-strips (respectively) from the reconstructed center for each event, again weighted by charge. The value of d_r for each event, is, in effect, a measurement of the event's width across the anode, which is a relevant difference between β and γ events.

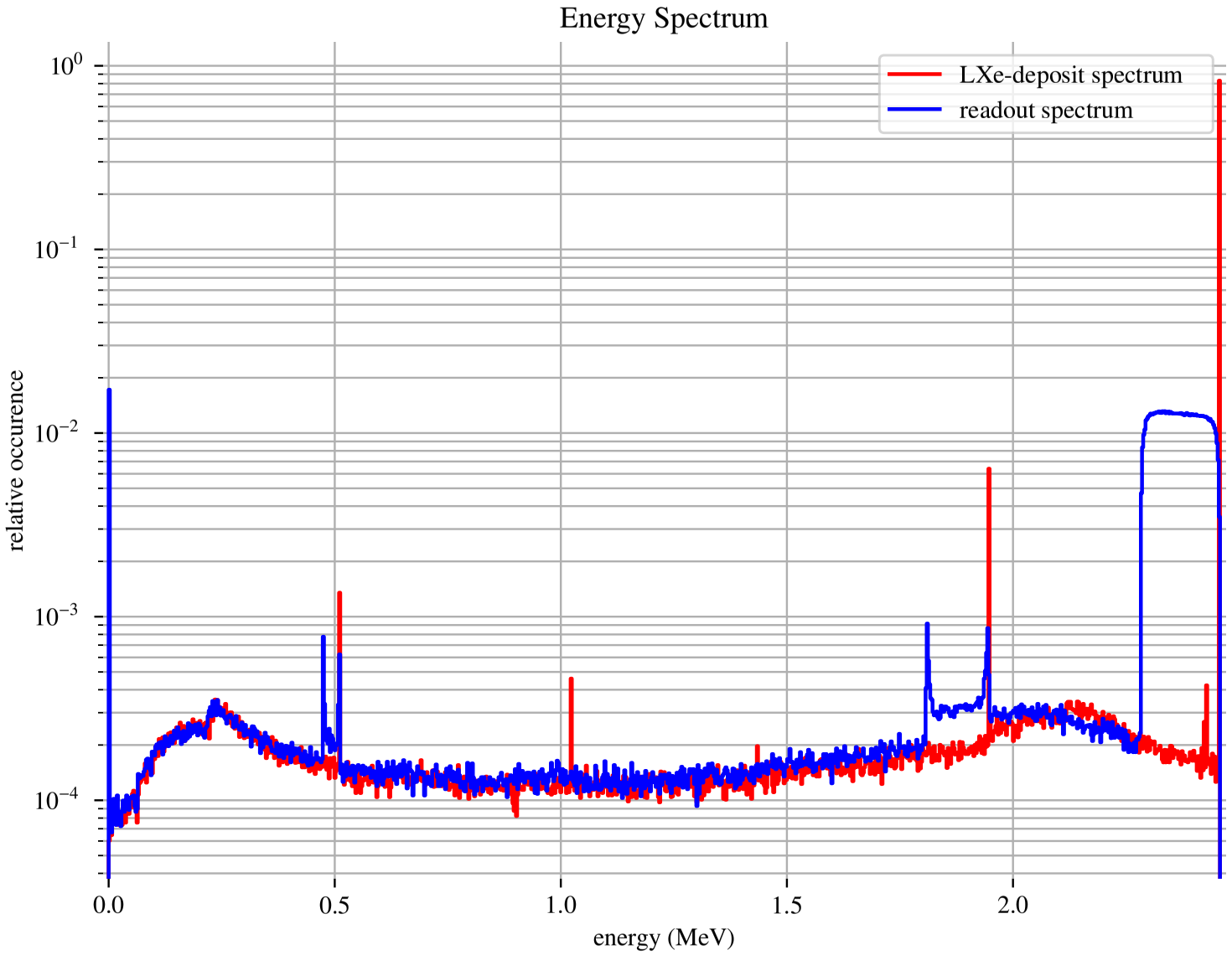

Figure 17: The energy spectrum of 1 million 2.4578 MeV γ events uniformly distributed in the TPC, with diffusion and the filter threshold disabled. This is similar to Figure 12, but with no tail on the low-energy side of peaks and plateaus. The single-escape and single-back-scatter peaks are split by their proximity to the TPC's outer walls, with the split-peaks representing the anode and cathode in particular.

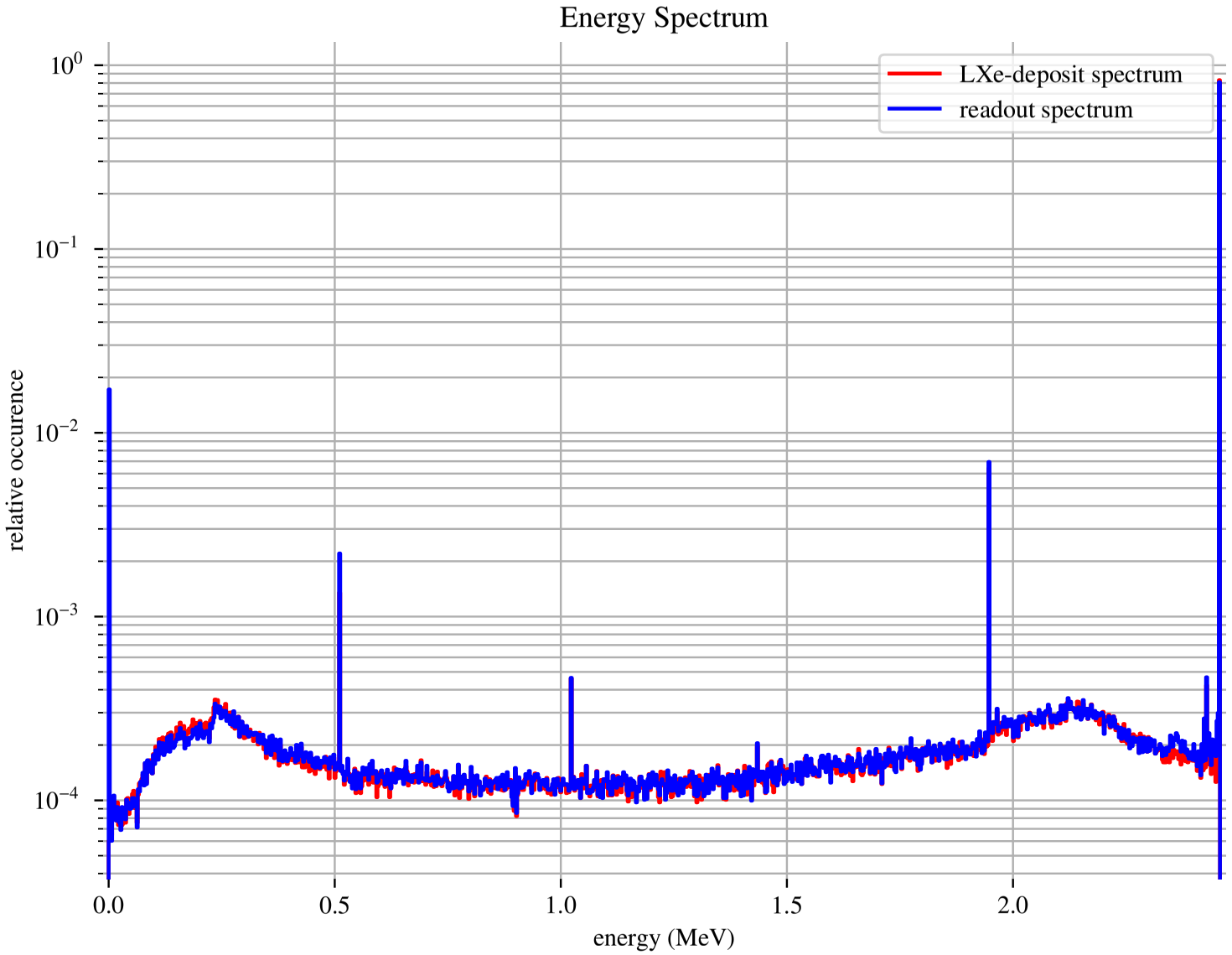

Figure 18: The energy spectrum of 1 million 2.4578 MeV γ events uniformly distributed in the TPC, with diffusion, the filter threshold, and impurity/attenuation disabled. The spectrum of the original deposits has been closely duplicated. A significant number of events remain excluded for being deposited entirely behind either the anode or cathode.

"Realistic" Comparison Parameters

Drift Parameters		Anode Parameters	
Trans. Diffusion	$0.0053\,\mathrm{mm^2\,\mu s^{-1}}$	Pad Width	3 mm
Long. Diffusion	$0.0013\,\mathrm{mm^2\,\mu s^{-1}}$	Strip Length	32 Pads
Drift Velocity	$1.89\,\mathrm{mm\,\mu s^{-1}}$	Noise	5.0 keV (200 e)
Purity	10 ms	Threshold	22.5 keV (900 e)
Other Parameters			
Event Distribution	plane 63.5 cm from anode	`readout` Algorithm	Gaussian
Event Energy	2.458 eV	Events Processed (`readout`)	400 000

Table 3: The initial set of validation parameters with which the `readout` package simulation was compared to an older version of the more-detailed simulation. This set of parameters was intended to be largely realistic: drift velocity and transverse diffusion were provided by Zepeng Li [26] for a drift field of $380\,\mathrm{V\,cm^{-1}}$, and are similar to the parameters used in Table 2. The standard deviation of the noise is 200 electrons at 25 eV per electron, while the threshold filter is 4.5 standard deviations of the noise. In both simulations, the sampling rate is set to 2 MHz, however since the comparison is for cumulative collection over time, this is not immediately relevant. Events were generated in a plane 63.5 cm from the anode.

Two sets of parameters have been used for comparison: the first (Table 3) was intended as a comparison for "realistic" parameters, while the second (Table 4) was intended as a parametric "stress-test". In both cases, two sets of events were also used: a set of γ-ray events and a set of single-β events, both with 2.458 MeV of energy per event and generated in a plane 63.5 cm from the anode. The use of two greatly differing sets of drift parameters was essential in properly understanding and matching the collection model to which the noise and threshold are applied in the more detailed simulation.

In Figures 19 to 22 are the first set of comparisons (Table 3) between the `readout` package and the more detailed simulation (with data from the latter provided by Zepeng Li [26]). The detailed simulation used a standard deviation of 200 electrons for noise, with a threshold filter of 900 electrons, which with a conversion ratio of 25 eV per electron gives a noise of 5 keV with a threshold of 22.5 keV. Deposits were collected by 3 mm pads. In each case, the `readout` package is in very

"Stress-Test" Test Parameters

Drift Parameters		Anode Parameters	
Trans. Diffusion	$0.01\,\mathrm{mm^2\,\mu s^{-1}}$	Pad Width	6 mm
Long. Diffusion	$0.001\,\mathrm{mm^2\,\mu s^{-1}}$	Strip Length	16 Pads
Drift Velocity	$1\,\mathrm{mm\,\mu s^{-1}}$	Noise	5.0 keV (200 e)
Purity	5 ms	Threshold	22.5 keV (900 e)
Other Parameters			
Event Distribution	plane 63.5 cm from anode	`readout` Algorithm	Gaussian
Event Energy	2.458 eV	Events Processed (`readout`)	400 000

Table 4: The alternate set of parameters with which validation of the `readout` package simulation was performed. Here, the standard deviation of the noise is 200 electrons at 25 eV per electron, while the threshold filter is 4.5 standard deviations of the noise. Events were generated in a plane 63.5 cm from the anode. The sampling rate remains 2 MHz.

good agreement with the detailed simulation, outside of an unexplained discrepancy in the fine structure of the peak for γ-ray widths (Figure 22).

To confirm that this agreement is consistent across varying parameter sets, comparisons were also made with a set of "stress-test" parameters (Table 4), shown in Figures 23 and 24. The agreement between the two simulations remains especially good. The slower drift velocity and higher transverse diffusion coefficient have increased the widths of collected events. Remaining deviations between the two simulations may be due to a small discrepancy in the transverse diffusion value used between the two simulation, or in the precise distance of the plane of generation from the anode. For example, adjusting the anode a single centimeter further away produces a slight amelioration in the agreement for β-events (Figure 25). Additionally a variant of Figure 23 with collection noise disabled has been included for comparison (Figure 26); at a close level of agreement, the disabling of noise has a marked effect on the sharpness of peaks and valleys in the distribution, without interfering with their alignment.

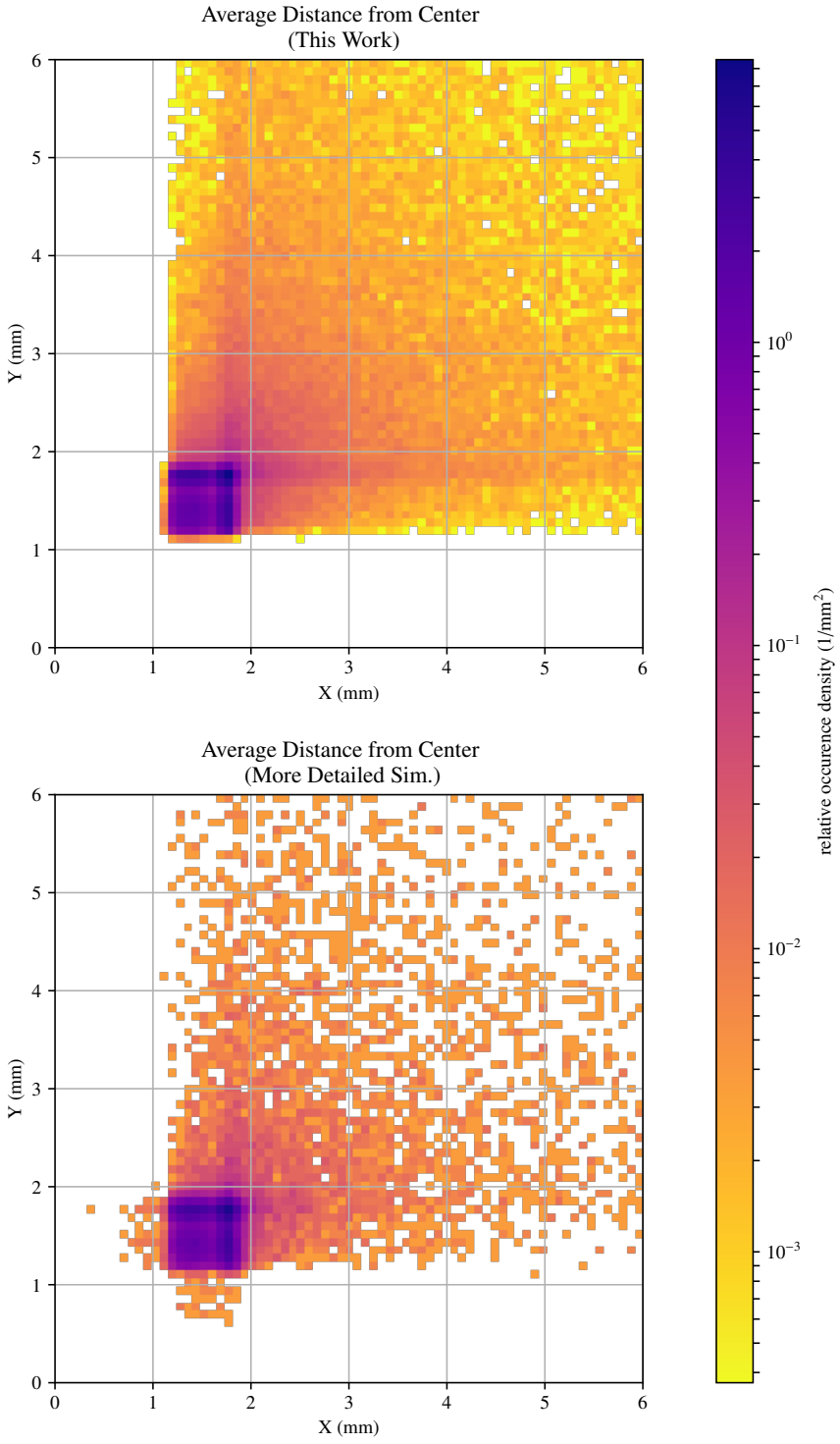

Figure 19: The average distance to the reconstructed center along x and y, independently (Equation 48), of 1 million 2.458 MeV β events (*top*) distributed on a plane 63.5 cm from the anode, with 3 mm pads (32 per strip), in comparison with 40 000 events from the more detailed simulation (comparison data; *bottom*), using the realistic simulation parameters from Table 3.

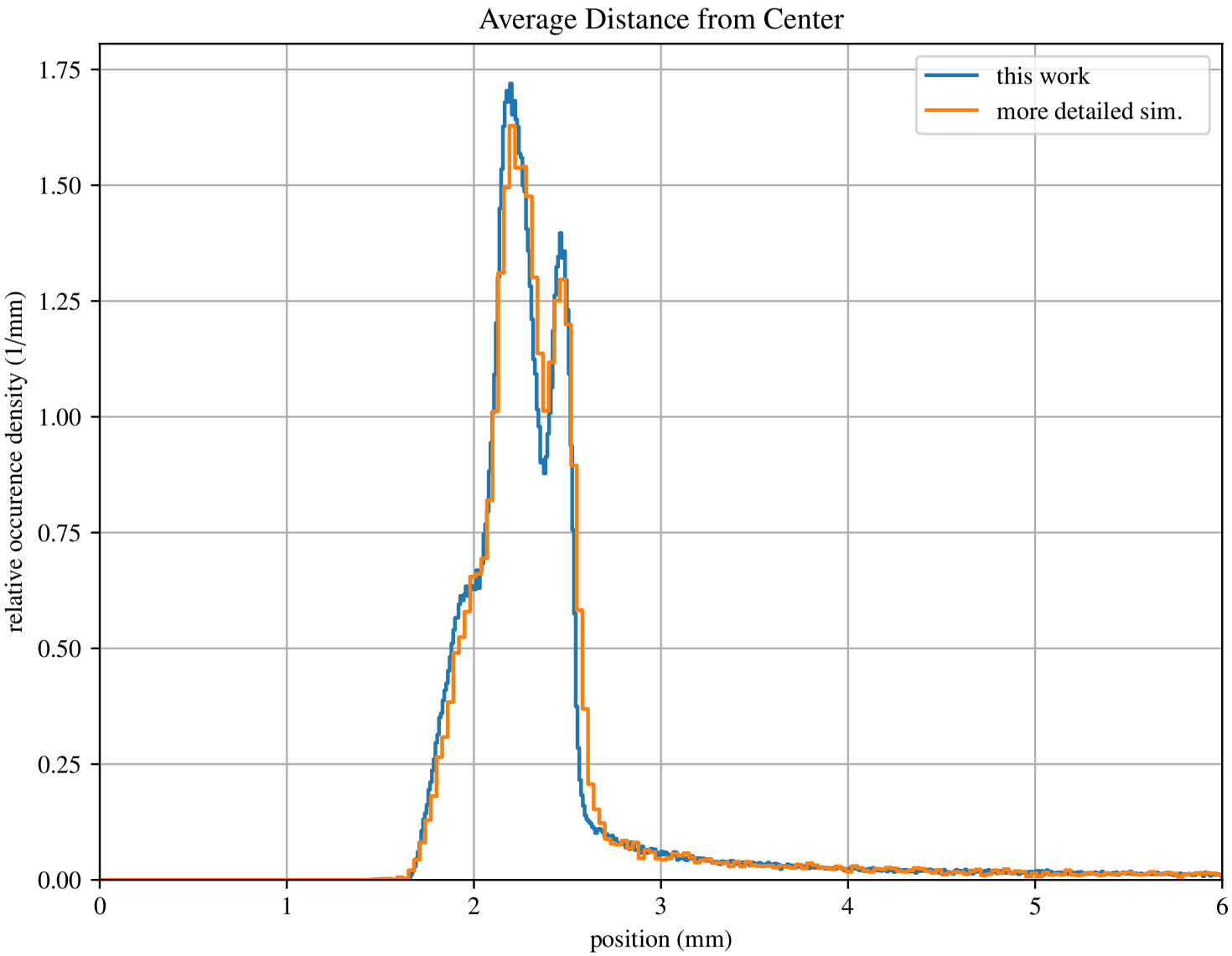

Figure 20: The average distance to the reconstructed center (Equation 49) of 1 million 2.458 MeV β events distributed on a plane 63.5 cm from the anode, with 3 mm pads (32 per strip), in comparison with 40 000 events from the more detailed simulation, using the realistic simulation parameters from Table 3.

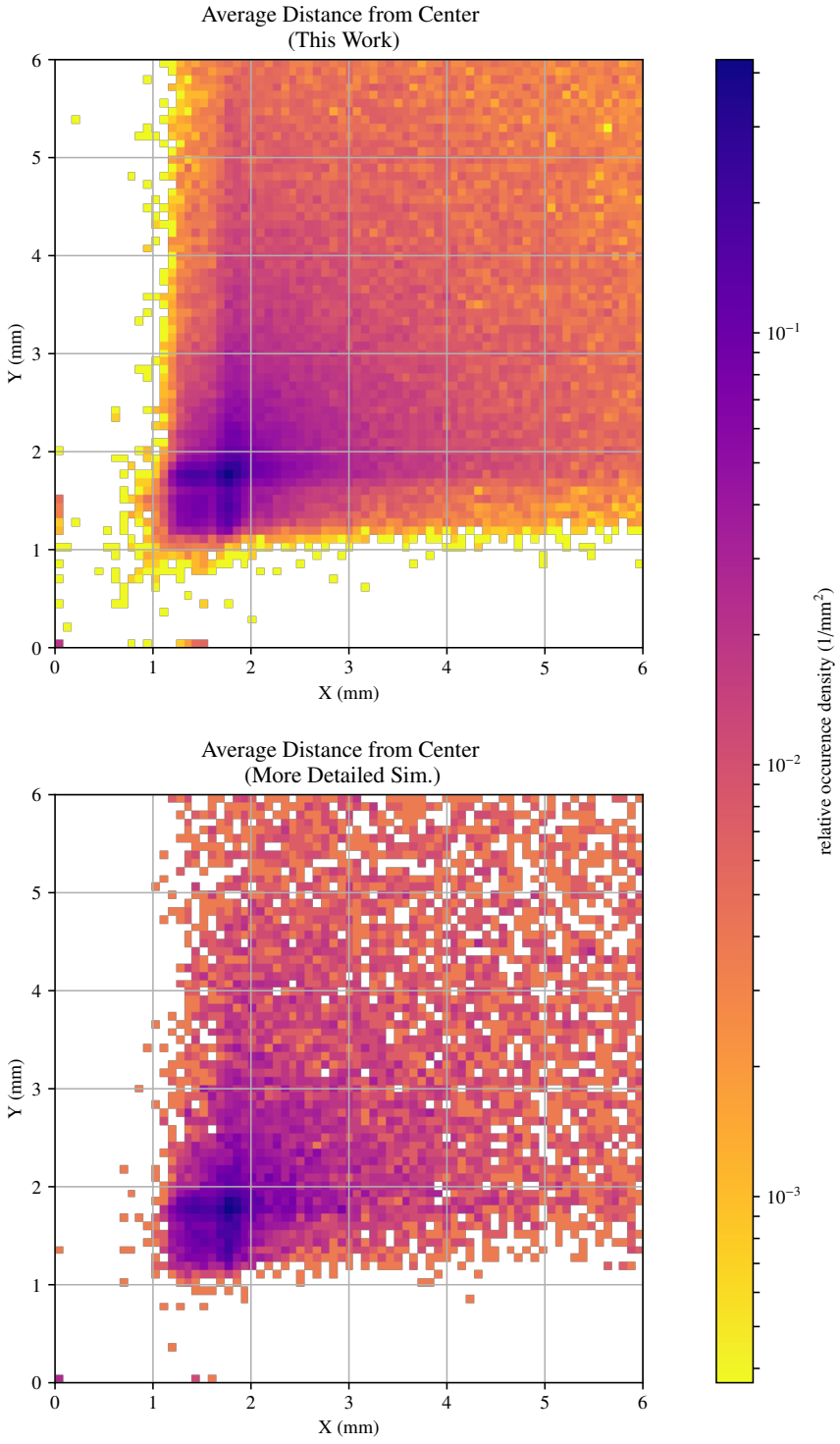

Figure 21: The average distance to the reconstructed center along x and y, independently (Equation 48), of 1 million 2.458 MeV γ events (*top*) distributed on a plane 63.5 cm from the anode, with 3 mm pads (32 per strip), in comparison with 40 000 events from the more detailed simulation (comparison data; *bottom*), using the realistic simulation parameters from Table 3.

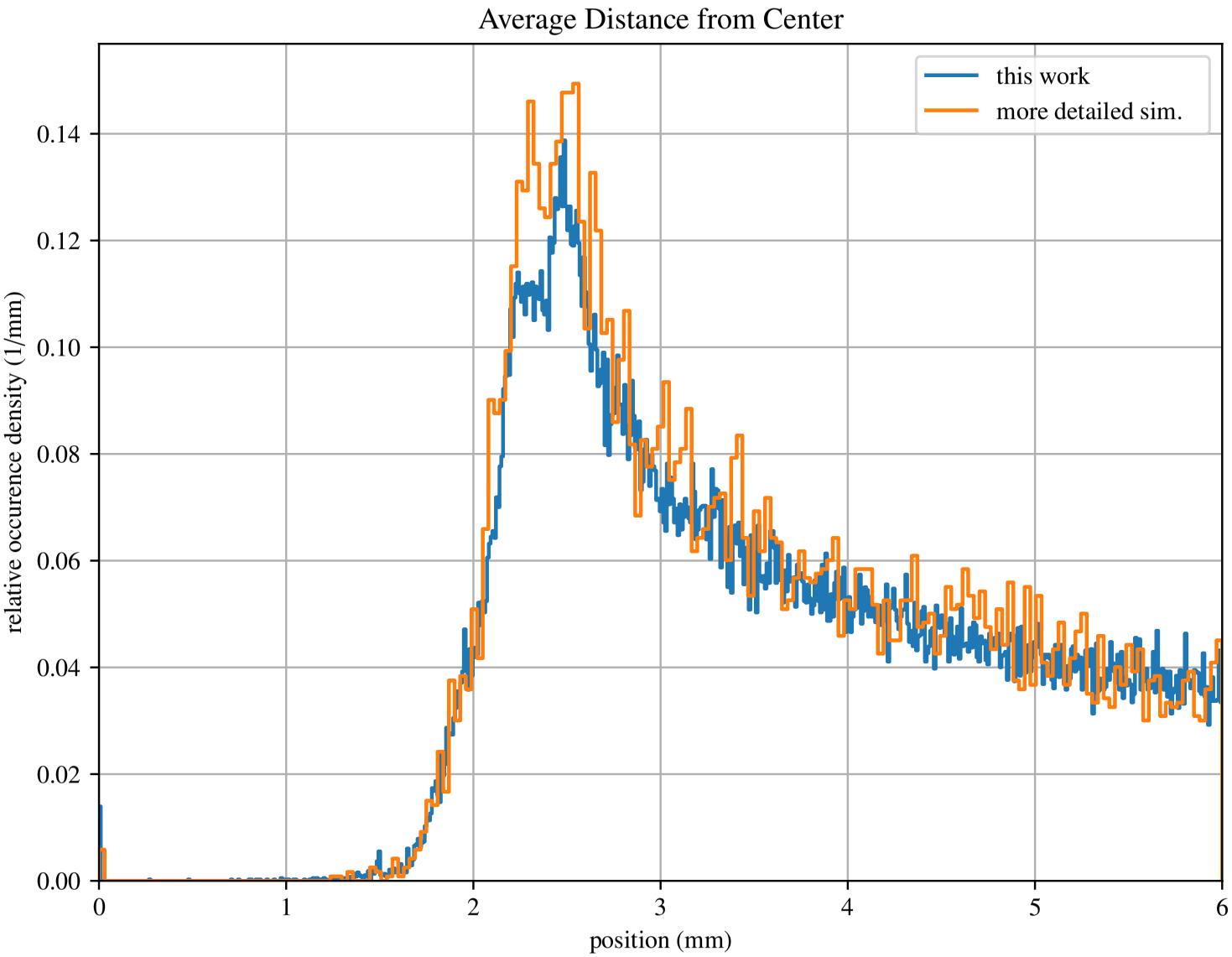

Figure 22: The average distance to the reconstructed center (Equation 49) of 1 million 2.458 MeV γ events distributed on a plane 63.5 cm from the anode, with 3 mm pads (32 per strip), in comparison with 40 000 events from the more detailed simulation, using the realistic simulation parameters from Table 3. The discrepancy in the peak structure is not currently understood.

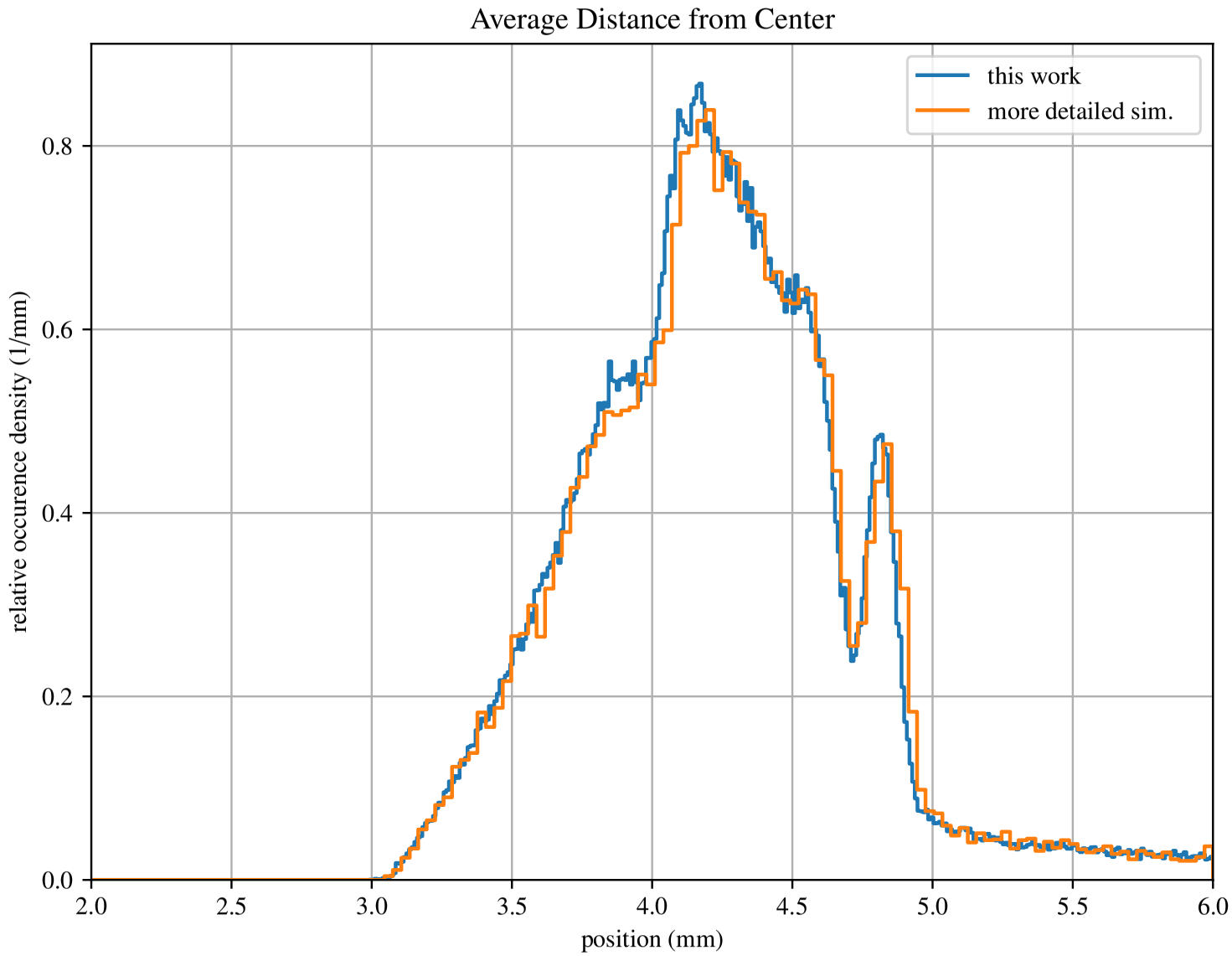

Figure 23: The average distance to the reconstructed center (Equation 49) of 400 000 2.458 MeV β events distributed on a plane 63.5 cm from the anode, in comparison with 39 800 events from the more detailed simulation, using the "stress-test" simulation parameters from Table 4.

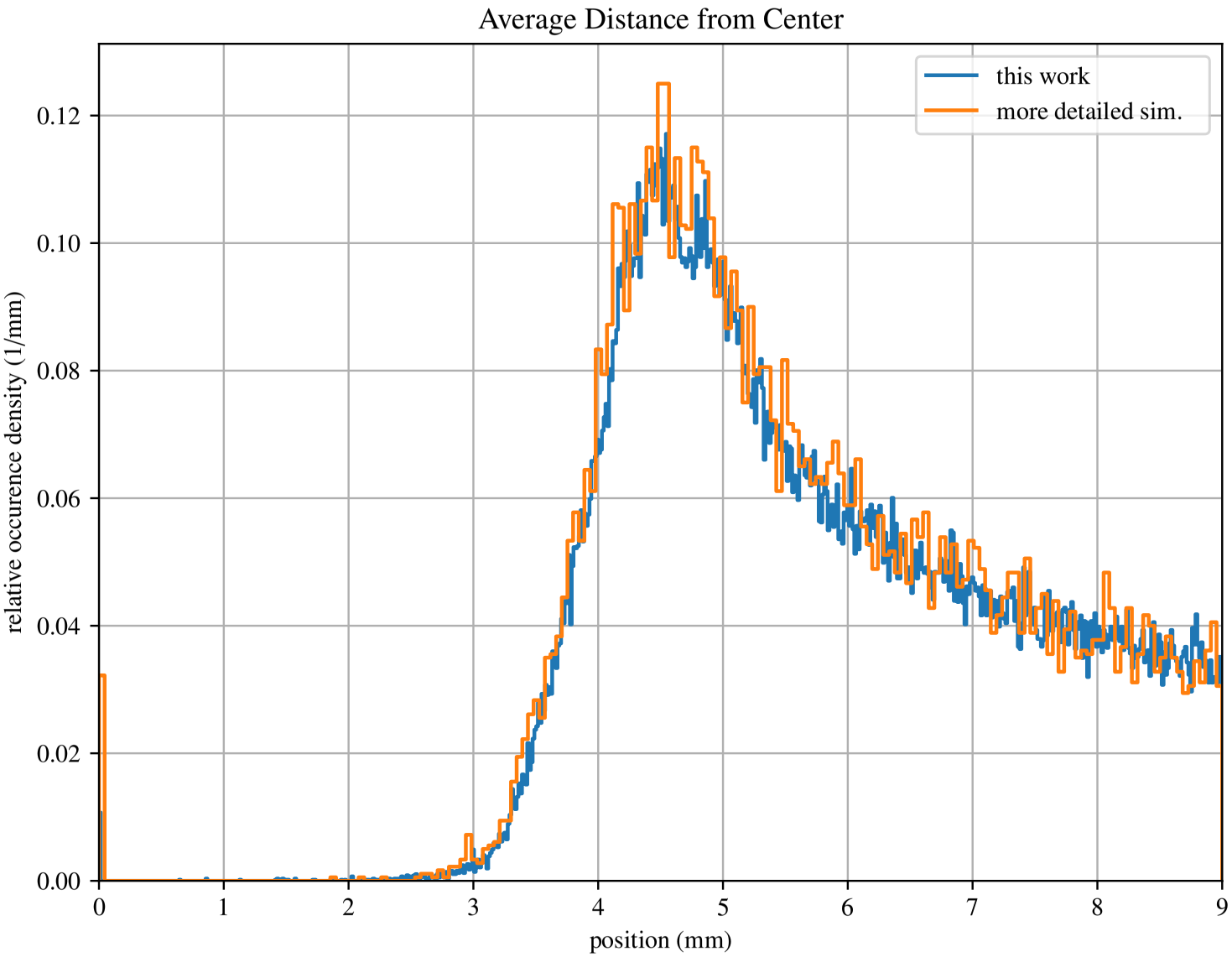

Figure 24: The average distance to the reconstructed center (Equation 49) of 400 000 2.458 MeV γ events distributed on a plane 63.5 cm from the anode, in comparison with 39 800 events from the more detailed simulation, using the “stress-test” simulation parameters from Table 4.

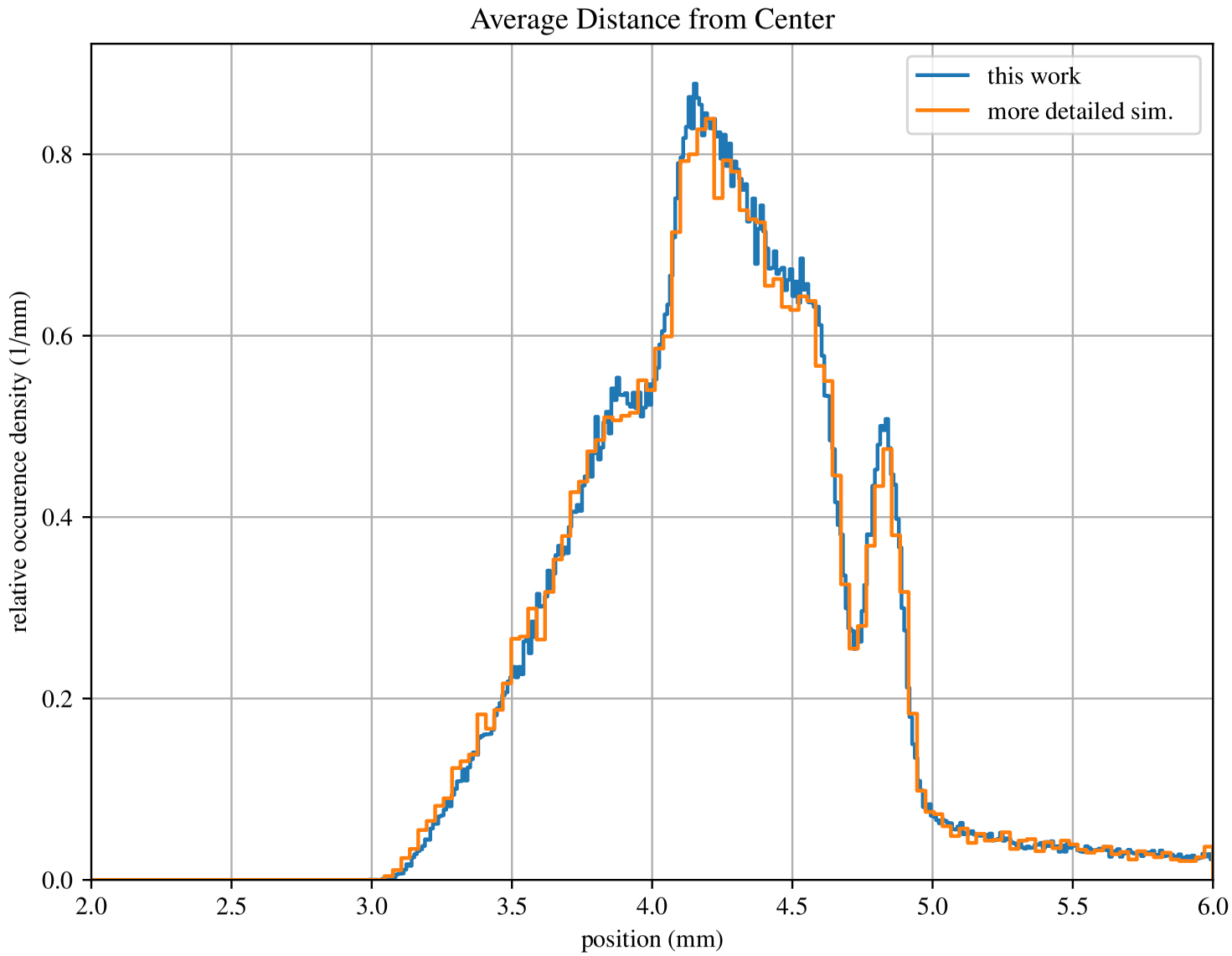

Figure 25: The average distance to the reconstructed center (Equation 49) of 400 000 2.458 MeV β events distributed on a plane 64.5 cm from the anode, in comparison with 39 800 events from the more detailed simulation, using the "stress-test" simulation parameters from Table 4. Compare with Figure 23; agreement is slightly improved in the alignment of the two peaks.

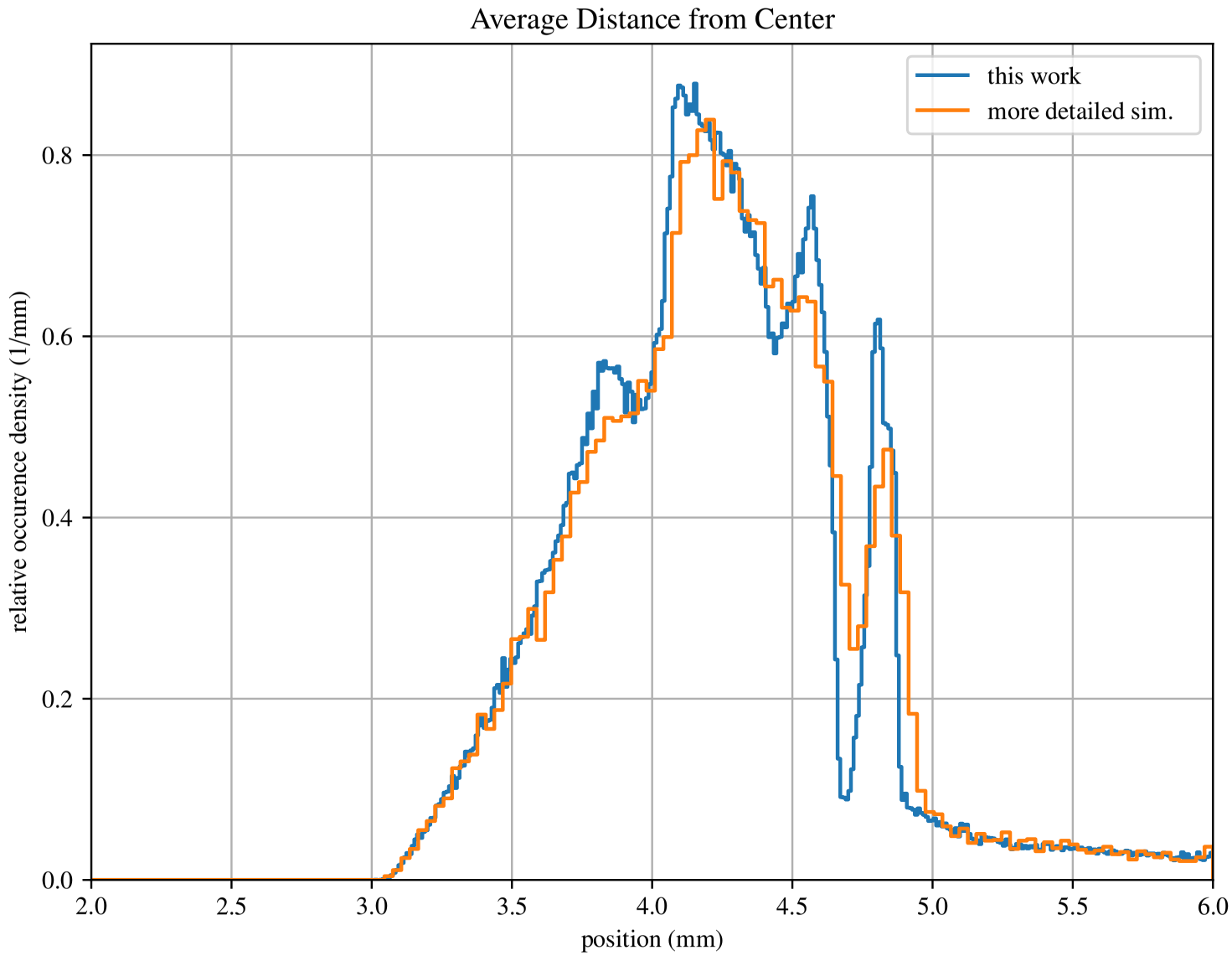

Figure 26: The average distance to the reconstructed center (Equation 49) of 400 000 2.458 MeV β events distributed on a plane 63.5 cm from the anode, in comparison with 39 800 events from the more detailed simulation, using the "stress-test" simulation parameters from Table 4, but with collection noise disabled. Compare with Figure 23; the peaks remain in position but with a much sharper resolution.

5 Conclusions

The `readout` package acceptably approximates charge collection in the nEXO TPC with good computational performance. Notable elements where there remains with room for improvement from future work include:

- The charge collection tiles will have spacing between them to allow for instrumentation. Spacing in integer pad-widths could be accomplished by discarding pads near edges of tiles, however, this would ignore the curvature of the electric field onto the tile edges, as the substrate is not strictly part of the anode. The gaps are also expected to be much smaller than the width of a pad, and thus with the curvature of the field may be ignorable for charge collection purposes [27].

- This package completely neglects the full time-varying behaviour of the surface-charge induction signal. The nature of this signal makes it inefficient to compute directly, due to the effect being spread across the entire anode until collection. However, certain values, such as the rise-time of the current waveform, are important in the determination of the axial topology of the charge cloud. Some comparable approximation, using the time-distributed collection data, will need to be devised.

- Energy deposited into real LXe produces both charge and light (scintillation), which are anticorrelated; a removal of energy prior to drift, potentially done either by preprocessing input tree or directly by the `readout` application, would be needed to better account for this. Performing this in preprocessing would allow the removed energy to be processed by the

fast-light simulation (a separate application), such that the outputs of the two applications would properly anticorrelate as well.

While the latter will be important in a final simulation pipeline including the `readout` package, it can be implemented externally to the package. The second will be statistically important for event-type discrimination, and the package has been designed to be easily extended to support this. The first is not considered to be of critical importance at this time.

References

[1] Pauli. *letter to Lise Meitner*. 1930. URL: http://cdsweb.cern.ch/record/83282.

[2] A. Bellerive et al. "The Sudbury Neutrino Observatory". In: *Nuclear Physics B* 908 (2016). Neutrino Oscillations: Celebrating the Nobel Prize in Physics 2015, pp. 30–51. ISSN: 0550-3213. DOI: 10.1016/j.nuclphysb.2016.04.035. arXiv: 1602.02469 [nucl-ex]. URL: http://www.sciencedirect.com/science/article/pii/S0550321316300736.

[3] R. Wendell et al. "Atmospheric neutrino oscillation analysis with subleading effects in Super-Kamiokande I, II, and III". In: *Phys. Rev. D* 81 (9 May 2010), p. 092004. DOI: 10.1103/PhysRevD.81.092004. arXiv: 1002.3471 [hep-ex]. URL: https://link.aps.org/doi/10.1103/PhysRevD.81.092004.

[4] nEXO Collaboration et al. "nEXO Pre-Conceptual Design Report". In: *ArXiv e-prints* (May 2018). arXiv: 1805.11142 [physics.ins-det].

[5] Steven R. Elliott and Petr Vogel. "DOUBLE BETA DECAY". In: *Annual Review of Nuclear and Particle Science* 52.1 (2002), pp. 115–151. DOI: 10.1146/annurev.nucl.52.050102.090641. arXiv: hep-ph/0202264. URL: https://doi.org/10.1146/annurev.nucl.52.050102.090641.

[6] S. M. Bilenky. "Neutrinoless double beta-decay". In: *Physics of Particles and Nuclei* 41.5 (Sept. 2010), pp. 690–715. ISSN: 1531-8559. DOI: 10.1134/S1063779610050035. arXiv: 1001.1946 [hep-ph]. URL: https://doi.org/10.1134/S1063779610050035.

[7] S. M. Bilenky and Carlo Giunti. "Neutrinoless double-beta decay: A brief review". In: *Modern Physics Letters A* 27.13 (2012), p. 1230015. DOI: 10.1142/S0217732312300157. arXiv: 1203.5250 [hep-ph]. URL: https://doi.org/10.1142/S0217732312300157.

[8] Stefano Dell'Oro et al. "Neutrinoless double beta decay: 2015 review". In: *Adv. High Energy Phys.* 2016 (2016), p. 2162659. DOI: 10.1155/2016/2162659. arXiv: 1601.07512 [hep-ph].

[9] C. E. Aalseth et al. "Search for Neutrinoless Double-β Decay in ^{76}Ge with the Majorana Demonstrator". In: *Phys. Rev. Lett.* 120 (13 Mar. 2018), p. 132502. DOI: 10.1103/PhysRevLett.120.132502. arXiv: 1710.11608 [nucl-ex]. URL: https://link.aps.org/doi/10.1103/PhysRevLett.120.132502.

[10] K. Alfonso et al. "Search for Neutrinoless Double-Beta Decay of ^{130}Te with CUORE-0". In: *Phys. Rev. Lett.* 115 (10 Sept. 2015), p. 102502. DOI: 10.1103/PhysRevLett.115.102502. arXiv: 1504.02454 [nucl-ex]. URL: https://link.aps.org/doi/10.1103/PhysRevLett.115.102502.

[11] M. Agostini et al. "Improved Limit on Neutrinoless Double-β Decay of ^{76}Ge from GERDA Phase II". In: *Phys. Rev. Lett.* 120 (13 Mar. 2018), p. 132503. DOI: 10.1103/PhysRevLett.120.132503. arXiv: 1803.11100 [nucl-ex]. URL: https://link.aps.org/doi/10.1103/PhysRevLett.120.132503.

[12] J. B. Albert et al. "Search for Neutrinoless Double-Beta Decay with the Upgraded EXO-200 Detector". In: *Phys. Rev. Lett.* 120 (7 Feb. 2018), p. 072701. DOI: 10.1103/PhysRevLett.120.072701. arXiv: 1707.08707 [hep-ex]. URL: https://link.aps.org/doi/10.1103/PhysRevLett.120.072701.

[13] A. Gando et al. "Search for Majorana Neutrinos Near the Inverted Mass Hierarchy Region with KamLAND-Zen". In: *Phys. Rev. Lett.* 117 (8 Aug. 2016), p. 082503. DOI: 10.1103/PhysRevLett.117.082503. arXiv: 1605.02889 [hep-ex]. URL: https://link.aps.org/doi/10.1103/PhysRevLett.117.082503.

[14] N. López-March and NEXT Collaboration. "Sensitivity of the NEXT-100 detector to neutrinoless double beta decay". In: *Journal of Physics: Conference Series* 888.1 (2017), p. 012243. arXiv: 1701.02697 [physics.ins-det]. URL: http://stacks.iop.org/1742-6596/888/i=1/a=012243.

[15] C. Patrick and F. Xie. "Status of the SuperNEMO $0\nu\beta\beta$ experiment". In: *Proceedings, Prospects in Neutrino Physics (NuPhys2016): London, UK, December 12-14, 2016*. 2017. arXiv: 1704.06670 [physics.ins-det].

[16] F. Alessandria et al. "Sensitivity and Discovery Potential of CUORE to Neutrinoless Double-Beta Decay". In: *ArXiv e-prints* (Sept. 2011). arXiv: 1109.0494 [nucl-ex].

[17] C. Alduino et al. "CUORE sensitivity to $0\nu\beta\beta$ decay". In: *The European Physical Journal C* 77.8 (Aug. 2017), p. 532. DOI: 10.1140/epjc/s10052-017-5098-9. arXiv: 1705.10816 [physics.ins-det]. URL: https://doi.org/10.1140/epjc/s10052-017-5098-9.

[18] Erica Caden. "Status of the SNO+ Experiment". In: *15th International Conference on Topics in Astroparticle and Underground Physics (TAUP 2017) Sudbury, Ontario, Canada, July 24-28, 2017*. 2017. arXiv: 1711.11094 [physics.ins-det].

[19] J. B. Albert et al. "Sensitivity and discovery potential of the proposed nEXO experiment to neutrinoless double-β decay". In: *Phys. Rev. C* 97 (6 June 2018), p. 065503. DOI: 10.1103/PhysRevC.97.065503. arXiv: 1710.05075 [nucl-ex]. URL: https://link.aps.org/doi/10.1103/PhysRevC.97.065503.

[20] Matthew Redshaw et al. "Mass and Double-Beta-Decay Q Value of ^{136}Xe". In: *Phys. Rev. Lett.* 98 (5 Feb. 2007), p. 053003. DOI: 10.1103/PhysRevLett.98.053003. URL: https://link.aps.org/doi/10.1103/PhysRevLett.98.053003.

[21] M Auger et al. "The EXO-200 detector, part I: detector design and construction". In: *Journal of Instrumentation* 7.05 (May 2012), P05010–P05010. DOI: 10.1088/1748-0221/7/05/p05010. URL: https://doi.org/10.1088%2F1748-0221%2F7%2F05%2Fp05010.

[22] J. B. Albert et al. "Searches for double beta decay of ^{134}Xe with EXO-200". In: *Phys. Rev. D* 96 (9 Nov. 2017), p. 092001. DOI: 10.1103/PhysRevD.96.092001. arXiv: 1704.05042 [hep-ex]. URL: https://link.aps.org/doi/10.1103/PhysRevD.96.092001.

[23] S. Agostinelli et al. "Geant4 - A Simulation Toolkit". In: *Nucl. Instrum. Meth. A* 506 (2003), pp. 250–303. DOI: 10.1016/S0168-9002(03)01368-8.

[24] Rene Brun and Fons Rademakers. “ROOT - An Object Oriented Data Analysis Framework”. In: *Nucl. Inst. & Meth. in Phys. Res. A*. Vol. 389. AIHENP’96 Workshop, Lausanne, Sep. 1996. 1997, pp. 81–86. URL: http://root.cern.ch/.

[25] *NEST*. URL: http://nest.physics.ucdavis.edu/.

[26] Zepeng Li. private communications. 2018.

[27] Dave Moore. private communications. 2018.

[28] Python Software Foundation. *Python Reference Manual*. 2018. URL: https://docs.python.org/3.6/reference/index.html.

[29] The SciPy community. *SciPy*. 2018. URL: https://scipy.org/.

[30] NumPy developers. *NumPy*. 2018. URL: http://www.numpy.org/.

[31] *Pandas*. 2018. URL: http://pandas.pydata.org/.

[32] Hunter et al. *Matplotlib: A 2D graphics environment*. 2007. URL: https://matplotlib.org/.

[33] E. Aprile and T. Doke. “Liquid xenon detectors for particle physics and astrophysics”. In: *Rev. Mod. Phys.* 82 (3 July 2010), pp. 2053–2097. DOI: 10.1103/RevModPhys.82.2053. arXiv: 0910.4956 [physics.ins-det]. URL: https://link.aps.org/doi/10.1103/RevModPhys.82.2053.

[34] *NEST Benchmark Plots*. URL: http://nest.physics.ucdavis.edu/benchmark-plots.

[35] J. B. Albert et al. “Measurement of the drift velocity and transverse diffusion of electrons in liquid xenon with the EXO-200 detector”. In: *Phys. Rev. C* 95 (2 Feb. 2017), p. 025502. DOI: 10.1103/PhysRevC.95.025502. arXiv: 1609.04467 [physics.ins-det]. URL: https://link.aps.org/doi/10.1103/PhysRevC.95.025502.

[36] Peter Sorensen. “Anisotropic diffusion of electrons in liquid xenon with application to improving the sensitivity of direct dark matter searches”. In: *Nuclear Instruments and Methods in Physics Research Section A: Accelerators, Spectrometers, Detectors and Associated Equipment* 635.1 (2011), pp. 41–43. ISSN: 0168-9002. DOI: 10.1016/j.nima.2011.01.

089. arXiv: 1102.2865 [astro-ph.IM]. URL: http://www.sciencedirect.com/science/article/pii/S0168900211001756.

[37] Samuele Sangiorgio. private communications. 2018.